High-Resolution 3D shallow S-Wave velocity structure of Tongzhou, subcenter of Beijing, inferred from multi-mode Rayleigh waves by beamforming seismic noise at a dense array

Qin Tongwei[1], Laiyu Lu[1], Zhifeng Ding[1], Xuanzheng Feng[1], and Youyuan Zhang[2]

[1]Institute of Geophysics, China Earthquake Administration
[2]Institute of Geophysics

November 24, 2022

Abstract

The 3D S-wave velocity of shallow structure, especially the Quaternary sediments at 0-1 km near the surface, is an important issue of concern in urban planning and construction for the requirements of seismic hazard assessment and disaster mitigation. Due to the facility and less dependence on the site environment, noise-based technique is an ideal way to acquire the fine structure of urban sedimentary basin. Based on the dense array composed of more than 900 stations deployed in Tongzhou at a local scale of 20×40 km^2, we proved the lateral variation of the phase velocity of multi-mode surface waves can be estimated directly with adequate accuracy by beamforming seismic noise with moving subarray, without tomography. Rayleigh wave phase velocity maps, at frequencies between 0.3 and 2.5 Hz for the fundamental mode as well as 0.8 and 3.0 Hz for the first overtone, are obtained. The 3D S-wave velocity model at 0-1 km depth with lateral resolution of 1 km is then established by inverting phase velocity maps of two modes. The thickness of the sediments is delineated by the impedance interface given by microtremor H/V (horizontal-to-vertical) spectral ratio. The model is in good agreement with tectonic unit. The sedimentary thickness of Daxing high and two sags located around Gantang and Xiadian are respectively 100-400 m and 400-600 m, which correlates well with the isosurface of S-wave velocity at 1 km/s. The model also presents some evidence on the extension of Daxing fault along NE direction.

High-Resolution 3D shallow S-Wave velocity structure of Tongzhou, subcenter of Beijing, inferred from multi-mode Rayleigh waves by beamforming seismic noise at a dense array

Tongwei Qin[1], Laiyu Lu[*1], Zhifeng Ding[1], Xuanzheng Feng[1] and Youyuan Zhang[1]

[1]Institute of Geophysics, China Earthquake Administration, Beijing,China

Correspondingauthor:Laiyu Lu (laiyulu@cea-igp.ac.cn)

Key Points:

- We proved the phase velocity of multi-mode Rayleigh wave can be extracted directly by beamforming the ambient noise with moving subarray
- A 3D *Vs* model of Tongzhou is established by inverting the phase velocity maps of the fundamental and the first overtone of Rayleigh wave
- The thickness of the sediments is delineated by the interface with strong impedance contrast obtained by H/V spectral ratio

Abstract

The 3D S-wave velocity of shallow structure, especially the Quaternary sediments at 0-1 km near the surface, is an important issue of concern in urban planning and construction for the requirements of seismic hazard assessment and disaster mitigation. Due to the facility and less dependence on the site environment, noise-based technique is an ideal way to acquire the fine structure of urban sedimentary basin. Based on the dense array composed of more than 900 stations deployed in Tongzhou at a local scale of 20 × 40 km^2, we proved the lateral variation of the phase velocity of multi-mode surface waves can be estimated directly with adequate accuracy by beamforming seismic noise with moving subarray, without tomography. Rayleigh wave phase velocity maps, at frequencies between 0.3 and 2.5 Hz for the fundamental mode as well as 0.8 and 3.0 Hz for the first overtone, are obtained. The 3D S-wave velocity model at 0-1 km depth with lateral resolution of 1 km is then established by inverting phase velocity maps of two modes. The thickness of the sediments is delineated by the impedance interface given by microtremor H/V (horizontal-to-vertical) spectral ratio. The model is in good agreement with tectonic unit. The sedimentary thickness of Daxing high and two sags located around Gantang and Xiadian are respectively 100-400 m and 400-600 m, which correlates well with the isosurface of S-wave velocity at 1 km/s. The model also presents some evidence on the extension of Daxing fault along NE direction.

Plain Language Summary

Large cities are usually built on the sedimentary basin, which can capture and amplify seismic energy and resulted larger damage. The main factors to determine the site amplification are the depth to the basement and the shear wave (S-wave) velocity of the sedimentary layer. We proposed a method to bulid the high-resolution 3D S-wave velocity model of the basin. The lateral variation of the Rayleigh wave phase velocity of the fundamental mode as well as the first overtone can be estimated directly with adequate accuracy by beamforming seismic noise with moving subarray, without tomographic inversion. 3D S-wave velocity model can thereby be established with high resolution by inverting the phase velocity maps of multi-mode surface waves. Meanwhile, the depth to the basement is delineated by the impedance interface given by microtremor horizontal-to-vertical spectral ratio. The fine structure of 3D S-wave velocity and the depth to the basement of Tongzhou, the subcenter of Beijing, is established using the data at a dense array composed of more than 900 stations using the proposed method. The model provides the information for seismic hazard assessment and disaster mitigation, which is generally the requirement in urban planning and construction.

1 Introduction

Sedimentary basins capture and amplify seismic energy. An important issue of concern for seismic hazard assessment is the amplification effect of the basin on the strong ground motion of earthquakes (Olsen, 2000), which is a subject for disaster mitigation in many cities around the world. S-wave velocity of the basin is a main factor affecting the amplification. Therefore, the 3D S-wave velocity of shallow structure, especially the Quaternary sediments at 0-1km near the surface, is required to understand the seismic response of sedimentary basin (Lai et al.2020). Moreover, unprecedented economic prosperity brought up the rapid development of large city. As a result, the construction of one or more sub-centers around the central city are planned to meet the increasing population growth which can not be carried by current city area. This is a main problem faced by many large cities in urban expansion. As a key element in detailed geological survey before construction, high-resolution 3D shallow S-Wave velocity structure under the ground would provide a guideline for urban planning on earthquake prevention and disaster reduction.

Seismic surface wave tomography is a main scheme for imaging the subsurface structure without invading the earth as done for drilling method and therefore is widly used in the field of near surface geophysical survey. S-wave velocity is usually obtained by inverting the dispersion curves of Rayleigh or Love wave in surface wave method. Different tomography technique can be found in early surface wave method, depending on the source type and the processing way for dispersion extraction. Spectral Analysis of Surface Wave(SASW) (Gucunski & Woods, 1992; Ganji et al., 1998) and Multichennel Analysis of Surface Wave(MASW) (Park et al., 1999) are two traditional methods using active source. In SASW, the dispersion of fundamental mode is extracted by cross-correlating the data recorded at two stations under the assumption the fundamental mode dominates the record. Apparent or effective dispersion curve, which is the average effect of multi-modes, is introduced to consider the existence of higher modes (Tokimatsu et al., 1992; Foti et al., 2011). However, extra calculation is required to obtain the effective dispersion curves of the predicted model to fit the observed one. MASW is then put forward and by which the separated dispersion of multi-modes can be estimated by f-k (Gabriels et al., 1987; Forchap & Schmid, 1998; Lu & Zhang, 2004), $\tau - p$ (McMechan & Yedlin, 1981; Forbriger, 2003a; 2003b).

However, the conduction of the method based on active source is limited by the complex circumstance of urban area. The excitation of active source or data collection usually can not be performed all over the area of interest. This limits the application of active source method in urban area especially when a 3D velocity model is supposed to be determined. Horizontal-to-vertical (H/V) spectral ratio of microtremor (Nakamura, 1989; 2019) and spatial auto-correlation (SPAC) (Aki, 1957) are two techniques based on passive source. Although there exists some controversy on the explanation, microtremor H/V are widely used in the field of engineer earthquake to estimate the sedimentary thickness and site amplification of the basin. H/V curve can also be used to invert for S-wave velocity by fitting it with Rayleigh wave ellipticity of the predicted model once the dominated record in microtremor is identified as the fundamental mode Rayleigh wave (Arai and Tokimatsu,2004).

SPAC is an array-based technique using passive source. Its theoretical basis was established as early as in 1957 when Aki(1957) found the azimuth average of the cross correlation of the microtremor recorded at two stations with distance r is the zero-order Bessel function $J_0(\omega r / c)$ of the first kind, where c is phase velocity, ω angular frequency, r the the spatial distance. In classic SPAC scheme, an array consisting of stations located at a circle with radius r and another one at the center is usually deployed. The velocity is estimated by fitting the observed SPAC coeffient with $J_0(\omega c / r)$ (e.g. Chávez-García and Luzón, 2005) or by picking zero-crossing point of the observed spectrum (Ekströmet et al., 2009; Nimiya et al., 2020; Salomón et al., 2021). This scheme proved to be also suitable for two stations and linear array (Chávez-García & Luzón, 2005; Chávez-García et al., 2006), or arrays with other geometry (Ohori et al., 2002). Similar to SASW, once the assumption the fundamental mode Rayleigh wave dominates the wavefield fails (Cho & Iwata, 2019), individual modes of Rayleigh wave can not be resolved by this scheme. Extra calculation on the apparent or effevtive phase velocity is needed in the inversion.

Benefit from the theory of seismic interferometry, some novel approaches based on ambient noise are developed to infer the earth structure at different scale. The basic principle of seismic interferometry is the Green's function between two stations can be retrieved by cross correlating their continuous noise record (Lobiks & Weaver, 2001; Campillo & Paul, 2003). Although this idea can date back to the pioneering work of Aki on SPAC (Aki, 1957; Chávez-García & Luzón, 2005; Tsai & Moschetti, 2010; Lu, 2021), revisiting and extensive research on ambient noise tomography provides new skills that are different from the passive method mentioned above. For instance, once the records of virtual source are constructed by calculating the noise cross-correlation function (NCF) of inter-stations, the traditional event-based tomography method at global or regional scale can be directly used to process the NCFs and invert for the velocity structure under the station network. The typical application is two-step surface wave tomography based on ambient noise, where 2D phase or group velocity map is constrained by pure-path inversion in the first step after extracting the velocity from NCFs (Yao et al., 2006). 3D S-wave velocity model is then obtained in second step by depth inversion. This method has also been used to infer the shallow structure at local-scale (Wang et al., 2017). The multi-mode cannot be resolved well when extracting the dispersion from NCFs along the raypath of inter-stations. This method is thereby often used for the situation where only the fundamental mode dominates.

Array-based scheme, such as SPAC (Yamaya et al., 2021), Fourier-Beseel transform (F-J) (Wang et al., 2019) and beamforming (Harmon et al., 2008; Roux & Ben-Zion, 2017; Wang et al., 2020), are proposed or redesigned to extract the multi-mode dispersion of surface wave based on new advance of seismic interferometry. Yamaya et al. (2021) proposed a variation of SPAC based on the fact that the SPAC is a statement in frequency domain for the same physics as the retrieval of Green's function by cross correlating the seismic noise. They estimate the velocity of multi-mode Rayleigh waves by comparing the observed cross-spectrum at an array with the theoretical SPAC coefficient. The 1D reference model under the array are inverted using the multi-mode dispersion curves and 3D velocity structure are obtained by investigating the perturbation relative to the reference one.

F-J method originated from the frequency expression of NCF of the same and/or cross components, which is related to the retrieval of tensor Green's function as stated by seismic interferometry theory (Wapenaar, 2004; Haney, 2012; Lu, 2021). According to the wave theory (Harkrider,1964; Ben-Menahem & Singh,1968; Chen,1999), the records at surface can be expressed as the Fourier Bessel integral with a kernel related to the structure and source parameters. The kernel can be written as a fraction composed of the numerator and denominator.

The integral contribution of the residues, which are determined by the roots make the denominator is zero, gives the surface wave. The kernel can thereby be obtained by taking the inverse Fourier-Beseel transform based on the virtual record of inter-stations. Aa a result, in f-v domain the peaks of the kernel would be associated to the eigenvalue of surface waves which make the denominator of the kernel is zero. The multi-mode dispersion can therefore be extracted by picking the peaks. This method was first proposed by Wang et al. (2019) based on the cross correlation of vertical component. Hu et al. (2020) extends this method to the correlation of cross components and also to extract dispersion of Love wave.

Beamforming is an array-based alternative to find the azimuth-averaged phase velocity under the array (Harmon et al., 2008) by measuring the spatial correlation of the phase information of a given plane wave across stations of an arrays (Rost and Thomas, 2002; Gerstoft & Tanimoto, 2007; Ruigrok et al., 2017). The phase velocity under the array can be estimated with minimal dependence on the distribution of noise sources and array geometry (Wang et al., 2020). If the azimuthal anisotropy is an issue, it can be measured as a function of azimuth (Löer et al, 2018) and the effect of source and array geometry can be corrected (Lu et al., 2018). With the deployment of large and dense networks, beamforming using different subsets of the stations of a larger network provides the opportunity to directly map phase velocity variations across the network without a tomographic inversion that is needed in two-step surface wave tomography. This scheme has already been successfully in the imaging at regional scale based on the data from Californian network (Roux & Ben-Zion, 2017) and ChinaAray (Wang et al., 2020), where only the fundamental Rayleigh mode is dominated. For surface waves, if more than one mode incident as a plane wave with far field approximation at velocity with much difference, the phase velocity of multi-modes can in principle be obtained by beamforming. This situation is more common in the local-scale, especially at the sedimentary basin where the energy of higher modes usually can not be omitted. The advantages considering higher modes in surface wave inversion are twofold. First, the inversion tends to be more stable and problem on multi-solution is conquered partly since more information is used to constrain the predicted model. Second, as the theory states for a given frequency the higher mode is more sensitive to the deeper structure than fundamental mode, and the deeper structure can then be inverted by considering higher modes at the same frequency range as that of fundamental mode (Xia et al., 2003).

In this study, we prove the phase velocity maps of multi-mode Rayleigh wave can be extracted directly by beamforming the ambient noise with moving subarray. We derive the 3D S-wave velocity structure of sedimentary basin at Tongzhou by the inversion of multi-mode Rayleigh waves. As an administration district, Tongzhou is located 30 km east of Beijing city and positioned as "the sub-center of Beijing" since 2013 to relieve the pressure of rapid development of Beijing. The thickness of the Quaternary sediment in Tongzhou is up to 600-700 m in some area. There are some active faults, including Xiadian fault where the large earthquake of ML 8.0 in 1679 is believed occur, passing through the study area. The 3D S-wave velocity structure near the surface would provide a guideline for the new city construction and disaster mitigation. We build the high resolution 3D S-wave velocity model at 0-1 km at local scale of 20×40 km^2 in Tongzhou based on the ambient noise at a dense array composed of more than 900 stations with interval about 1 km. We first divided the array into subarrays with overlapping. For each subarray, we use beamforming method to measure the phase velocity of fundamental mode as well as the first higher mode. The 2D phase velocity maps of two modes are directly obtained without tomographic inversion. The 3D fine S-wave velocity model is then built by depth inversion of multi-mode dispersion curves for each subarray. Moreover, we use the H/V spectral ratio to delineate the thickness of the sediments, which is described by the interface with strong impedance contrast given by the resonance frequency of H/V spectral ratio.

The paper is organized as follows: the tectonic and geological setting are first introduced in section 2. The data and method for measuring phase velocity is briefly described in section 3. In section 4, the characteristics of the phase velocities and 2D phase velocity maps are investigated both for the fundamental mode and the first overtone. 3D S-wave velocity model with high resolution is then established in section 5 by depth inversion of multi-mode Rayleigh waves. Tectonic implications and the thickness of sediments from H/V ratio are also discussed section 5. Conclusions are given in section 6.

2 Tectonic and geological setting

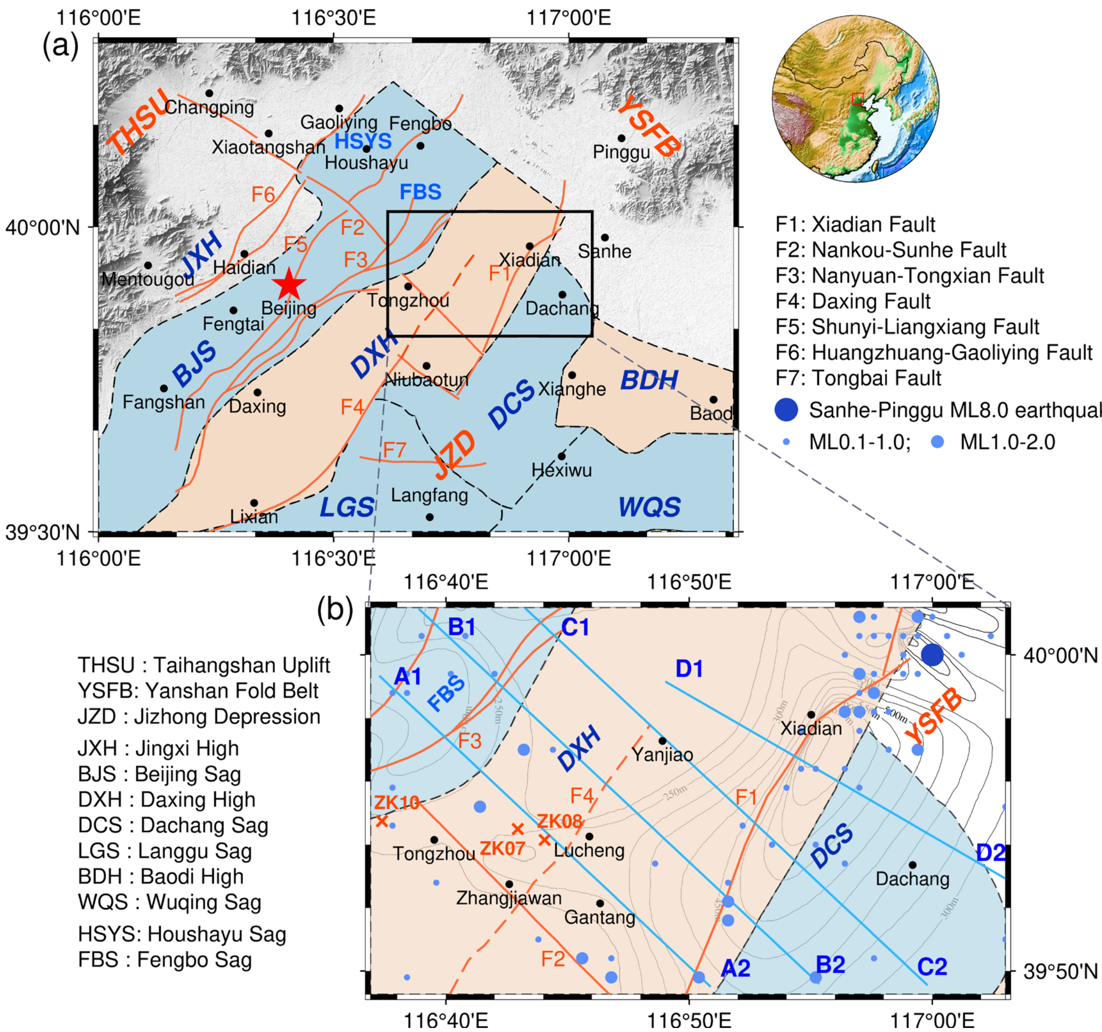

Figure 1. The geological setting of the study area. The distribution of the faults (orange solid line) is adapted from Xu et al. (2016). The tectonic units and its boundary (black dashed line) are adapted from Gui et al. (2017). The cross sections A1-A2, B1-B2, C1-C2 and D1-D2 are discussed in Section 5. ZK07, ZK08 and ZK10 are locations of three boreholes which come from Lei et al.(2021). The earthquakes occurred in the area from 1900-2021 are taken from the unified earthquake catalog of China from CENC (China Earthquake Networks Center). The black thin lines in (b) are the isopach of Quaternary sediments. The orange dashed line is supposed to be the northeast extension of Daxing fault, inferred from our model, which is discussed in section 5.4.

On a regional scale, as shown in Figure 1a, the study area is located in the transition zone between the North China Basin (NCB) and the Yanshan Fold Belt (YSFB). The western portion is the Taihangshan Uplift (THSU). As the first-order tectonic unit, North China Basin is a large epicontinental basin which is characterized by alternate uplift and depression zones with NE-SW direction (Hellinger et al., 1985; Ye et al., 1985; Huang and Zhao, 2004). The study area is mainly located the secondary tectonic unit of NCB named Jizhong Depression (JZD), except a small area in the northeast which enter the YSFB.

On a local scale, the study area is named Beijing plain, located on the northwestern margin of the North China Basin, with NE-SW striking faults as the main structure. Since the Tertiary, a tectonic pattern with alternate sag and high was formed in Beijing plain, namely the Jingxi high (JXH), Beijing sag (BJS) and Daxing high (DXH) (Huang et al.,1991). Dachang sag (DCS), administratively belongs to Hebei province, is located in the southeast of the study area, adjacent to Daxing high.

Since the Quaternary, under the influence of the Yanshan movement, due to the tensile stress field at NW-SE direction, new feature has shaped the extensional tectonic in this area. The activity of Nankou-Sunhe fault (F2) with NW-SE striking cut the tectonics with NE-SW direction. The portion of Beijng sag located in the northeast of the Nankou-Sunhe fault is decomposed two sags named Houshayu sag (HSYS) and Fengbo sag (FBS), which are bounded by the Shunyi-Liangxiang fault (F5).

NE-striking faults, such as Nanyuan-Tongxian fault (F3), Xiadian fault (F1) and Daxing fault (F4), are usually recognized the boundary of the tectonic unit. The Nanyuan-Tongxian fault is the boundary between the BJS and DXH. As a secondary tectonic unit of the BJS, the FBS is located in the northwest of the study area, to the northwest of the Nanyuan-Tongxian fault. The DXH and DCS are bounded by the Xiadian fault, which is generally recognized to be a Holocene active normal fault.

Daxing fault (F4) is the boundary between the DXH and Langgu sag (LGS). It is generally believed that this fault extends along NE direction and ends at Niubaotun, where it is connected to the Xiadian fault with an arc shape. New study shows (He et al., 2020) the Daxing fault would extend northeast and enter our study area, as shown by the orange dashed line in Figure 1b. The Nankou-Sunhe fault (F2) with NW-striking, the southeast section of which is located in the study area, controls the formation and development of the HSYS and FBS. This fault, as well as the Nanyuan-Tongxian fault (F3), has an important effect on the deposition of the DXH.

The study area has always been a seismic zone owing to the strong tectonic activities and the development of active faults. Meanwhile, large disaster would be caused by the earthquake due to the dense population in this area. Figure 1b shows the distribution of earthquakes that occurred in the area since 1900. In particular, the ML8.0 Sanhe-Pinggu earthquake in 1679 occurred on the Xiadian fault in the study area. In addition, the area is covered by loose Quaternary sediments, and which has a greater impact on seismic waves as a result of site effect. The 3D S-wave velocity model with high-resolution and the depth to the basement would be helpful for the study on site response and thereby for the disaster reduction.

3 Data and Mehod

Since the dense array with large aperture is available now, the beamforming can be used to the subarray and the phase velocity map can then be directly obtained without tomographic inversion by moving the subarray. Moving-array beamforming has been successfully for the case that fundamental mode Rayleigh wave dominate the record (Roux & Ben-Zion, 2017; Wang et al., 2020). Based on NCFs between vertical-vertical component we show in this paper it is also valid for the case that more than one mode dominate the record.

3.1 Data

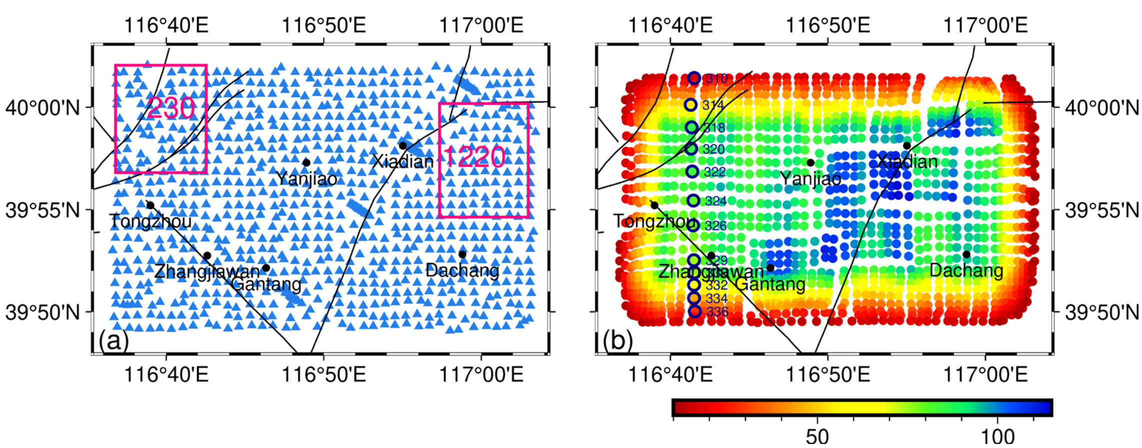

Figure 2. (a) The station distribution of Tongzhou dense array, which are denoted by triangles. The analysis of subarray 230 framed by a box is given as an example in Figures 3, 4 and 5. (b) The reference locations of total 1485 subarrays. The number of stations involved in each subarray is denoted by the color. The dispersion image of subarrays highlighted by circles in (b) are shown in Figures 7.

The data we are using comes from the Tongzhou dense array consisting of 919 stations which are conducted from November 20, 2019 to January 3, 2020, with a synchronized observation duration of 45 days. The station distribution is given in Figure 2a. The interval between the neighboring station is about 1 km. Two types of short-period seismometers, EPS, with a corner frequency of 5 s and CQS, with a corner frequency of 20 s, were involved in the observation. The sampling frequency is 200Hz.

Following the procedures described in Bensen et al. (2007), we first resample the data with 20 Hz, remove trend and mean. We then divide the data into 1-h segments and apply one-bit normalization to limit the effect of transients like local or teleseismic earthquakes. The NCFs of inter-stations were calculated and stacked. Since only the Rayleigh waves are studied, only the NCFs of vertical-vertical components are considered in this paper.

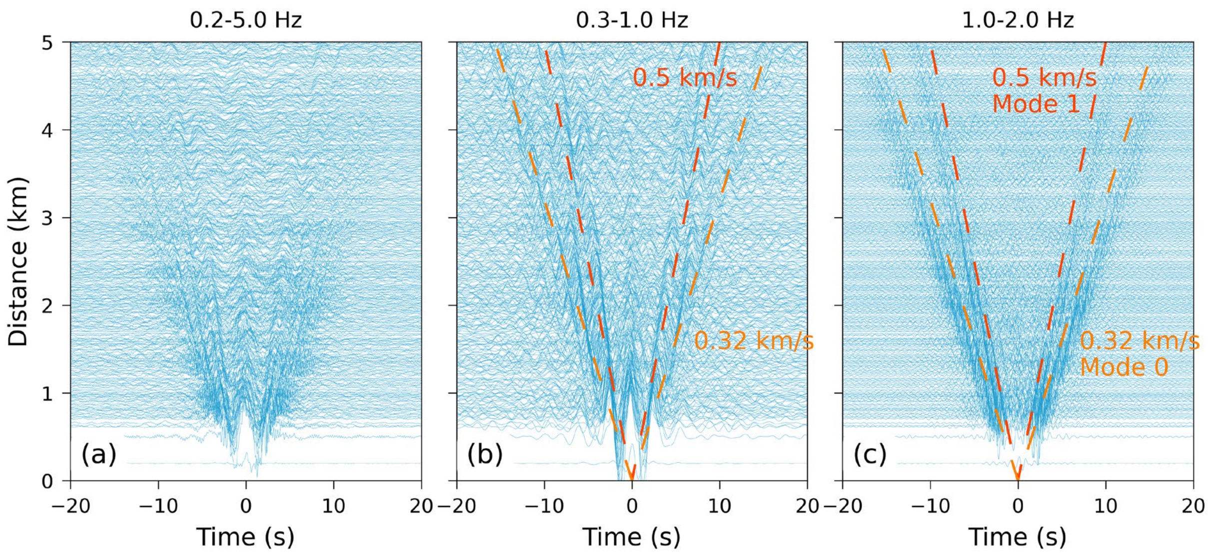

Figure 3. Noise correlation functions between vertical-vertical component for the inter-stations inside the subarray 230 shown in Figure 2 with band-pass filter 0.2-5.0 Hz (a), 0.3-1.0 Hz (b) and 1.0-2.0 Hz (c), respectively. Dashed lines in (b) and (c) denote the arrival time with the labeled group velocity. Two separated modes are visible in (c).

As an example, Figure 3 gives the vertical-vertical NCFs of inter-stations located inside the subarray of 230 framed in Figure 2, which are filtered with different bandpass filters. Figure 2(c) shows two separated modes can be clearly seen for the waves with bandpass filter of 1.0-2.0 Hz. This implies the dispersion curves of two modes can be expected for extraction by beamforming. Due to the longer wave length and smaller velocity difference, mode separation is ambiguous in Figure 3a and 3b for low frequency range.

3.2 Cross-correlation Beamforming

Similar to most array-based method, it is assumed the wave arrive the array with a plane wavefront. Beamforming is then designed to track the phase of the wave with a given azimuth and slowness (Rost & Thomas, 2002). Most applications of surface wave beamforming have been done using earthquake data, ambient noise can in principle also be used and yield primarily information on Rayleigh wave propagation since the dominant Rayleigh wave can be retrieved by cross correlating the continuous ambient seismic noise. The expression for the cross-correlation beamforming (CCBF) in the frequency domain can be expressed as (Ruigork et al., 2017)

$$B\left(p,\theta,\omega\right)=\left|\sum_{i=1}^{n}\sum_{j=1}^{n}e^{\iota \boldsymbol{x}_i\cdot\boldsymbol{k}}d\left(\boldsymbol{x}_i,\omega\right)\left[d\left(\boldsymbol{x}_j,\omega\right)\right]^{*}\left[e^{\iota \boldsymbol{x}_j\cdot\boldsymbol{k}}\right]^{*}\right| \qquad (1)$$

where B represents beamforming result and $p=1/v$ represents horizontal slowness. v is the phase velocity of the monochromatic plane wave, θ back azimuth, $\omega=2\pi f$ the angular frequency and f frequency. $\boldsymbol{e}^{\iota \boldsymbol{x}_i\cdot\boldsymbol{k}}$ represents the phase delay of station i at $\boldsymbol{x}_i$ relative to the plane wave $k=\omega p\left(\sin\theta,\cos\theta\right)$ at the center of the array. Superscript * represents the conjugate transpose. $d\left(\boldsymbol{x}_i,\omega\right)$ is the Fourier spectrum of the record at station $\boldsymbol{x}_i$ and $d\left(\boldsymbol{x}_i,\omega\right)\left[d\left(\boldsymbol{x}_j,\omega\right)\right]^{*}$ is thus the cross-spectral density between station $\boldsymbol{x}_i$ and $\boldsymbol{x}_j$, which is associated to the NCFs in the time domain.

Figure 4 shows the beamforming output for the subarray 230 labeled by a box in Figure 2a where 79 stations are involved. The beamforming result is plotted as a function of phase velocity and azimuth. The dashed lines denote the isophase velocity with the labeled value. Figures 4a and 4b are the results for the single frequency of 0.5 and 1.0 Hz. Figures 2c and 2d are the results for the frequency band of 0.4-0.6 Hz and 0.8-1.2 Hz. In each panel, the results are normalized by the maximum. As expected, a nearly continuous circle with phase velocity about 1 km/s can be seen at 0.5 Hz in Figure 4a. Although the energy may vary with the azimuth due to the source distribution and station-pair orientation, this circle can also be identified in Figure 4c for the frequency band 0.4-0.6 Hz with broaden extension caused by dispersion. Figure 4b shows two circles with phase velocity of 0.5 km/s and 0.8 km/s can be distinguished at 1.0 Hz and the broaden energy belt near these two circles can also be observed for the frequency range 0.8-1.2 Hz, as expected. Nearly continuous distribution along the circles, which are identified as the fundamental and first higher mode, indicates a relatively uniform noise source distribution without dominant azimuth. In addition, Figure 4b and 4d shows the beamforming result of the first higher mode with high velocity is significantly larger than that of the fundamental one.

Chmiel et al. (2019) also found similar results, where they detected the higher mode Rayleigh wave in the basin of the Groningen gas by beamforming the ambient noise.

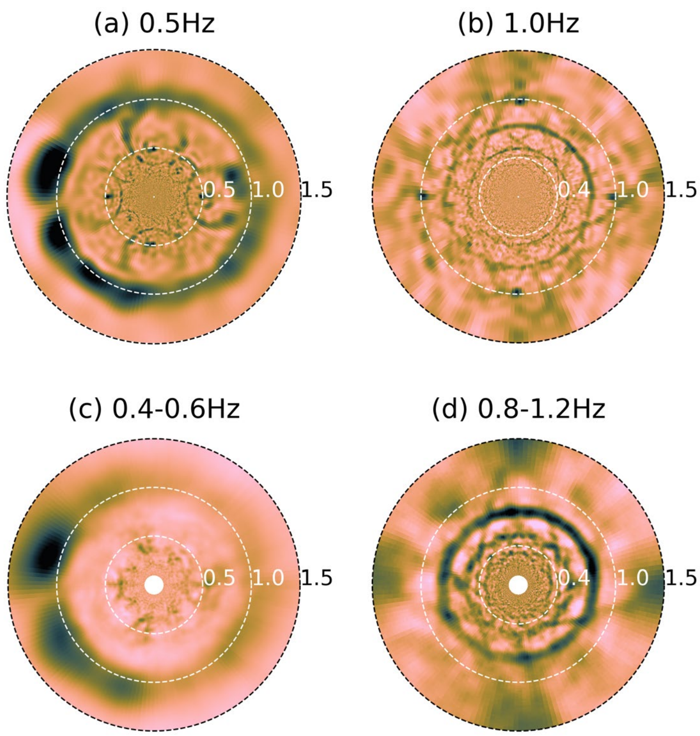

Figure 4. The beamforming result as a function of phase velocity and azimuth for the subarray 230 shown in Figure 2a. 79 stations are involved in this subarray. The dashed line denotes the isophase velocity of labeled value (unit: km/s). (a) and (b) are the result for single frequency of 0.5 and 1.0 Hz. (c) and (d) are the result for the frequency band of 0.4-0.6 and 0.8-1.2 Hz. The results are normalized by the maximum of each panel.

To calculate the beamforming result shown in Figure 4, the cross-spectral density in equation (1) is calculated using the Fourier spectrum of the NCFs shown in Figure 3. However, it should be pointed out the beamforming can be performed in the frequency domain by taking the raw noise data as the input. The calculation and output of NCFs is not necessary in principle since the extraction of the dispersion curve by beamforming does not depend on NCFs, as opposed to the frequency-time analysis for traditional two-station surface wave method where the output of NCFs is essential.

3.3 Extraction of multi-mode dispersion

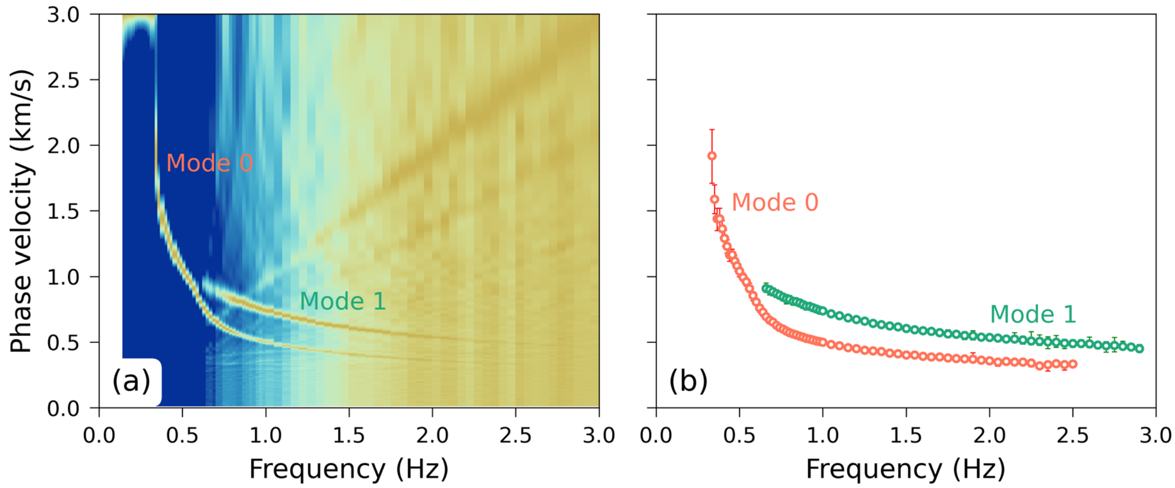

Figure 5. Illustration of the extraction of the azimuth-averaged phase velocity by beamforming the ambient noise inside the subarray 230 shown in Figure 2a. (a) The azimuth-averaged beamforming result obtained by combining the results for all frequencies of interest. For each frequency, the beamforming result is normalized by the maximum. (b) The phase velocity dispersion branches picked at the peak of the beamforming result. The error bar is based on the bandwidth of ±0.95 maximum beamforming energy.

The process of dispersion extraction for single mode is similar as that described in Wang et al. (2020). The dependence of the velocity on the azimuth is not considered at present. We average the beamforming energy shown in Figures 4a or 4b over the azimuth for each frequency and combine the results of each frequency into the frequency-velocity (f-v) domain, as shown in Figure 5a, where two dispersion branches labeled by mode 0 and mode 1 are clearly observed. For each frequency, the azimuth-averaged phase velocity is then extracted by picking the value corresponding to the peaks of the beamforming energy. The error is estimated by calculating the width of the phase velocity range where the energy is at 95% of the maximum($0.95EBW$). The final estimation on the phase velocity of two modes are as shown in Figure 5b.

We then apply the same process to all subarrays to extract the azimuth-averaged phase velocity at each frequency under the subarray. The study area is parameterized by $0.1° \times 0.1°$ subarrays with 0.01° overlapping. The choice of the subarray aperture and the size of the overlap is a trade-off between the velocity accuracy, which mainly depends on the station number involved in the subarray, and the lateral resolution, which depends on the size of the overlap, as well as the aperture of the subarray. The investigation on beamforming resolution and phase velocity uncertainty can refer to the discussion in Wang et al. (2020). The current parameterization is selected after testing different schemes and it has been proved to be able to meet our requirements for lateral resolution and target depth. Total 1485 subarrays are finally analyzed. For each subarray, the velocity is regarded as the average velocity at the reference location, which is calculated by averaging coordinates over the stations inside the subarray. Therefore, the reference point, which depends the geometry of the station distribution inside the subarray, is usually not the geometric center of the square subarray. Especially at the area near the XiaDian fault, where 4 denser linear arrays perpendicular to the fault striking are designed and as a result, the reference point tends to be close to the location of the denser linear array. Figure 2b shows all reference point of all subarray and the number of stations involved of each subarray, which is usually between 10 and 115. There are more than 50 stations for most subarray except the one at the edge of the study area. Figure 2b can be used to qualitatively assess the reliability of the velocity and resolution capability of the result.

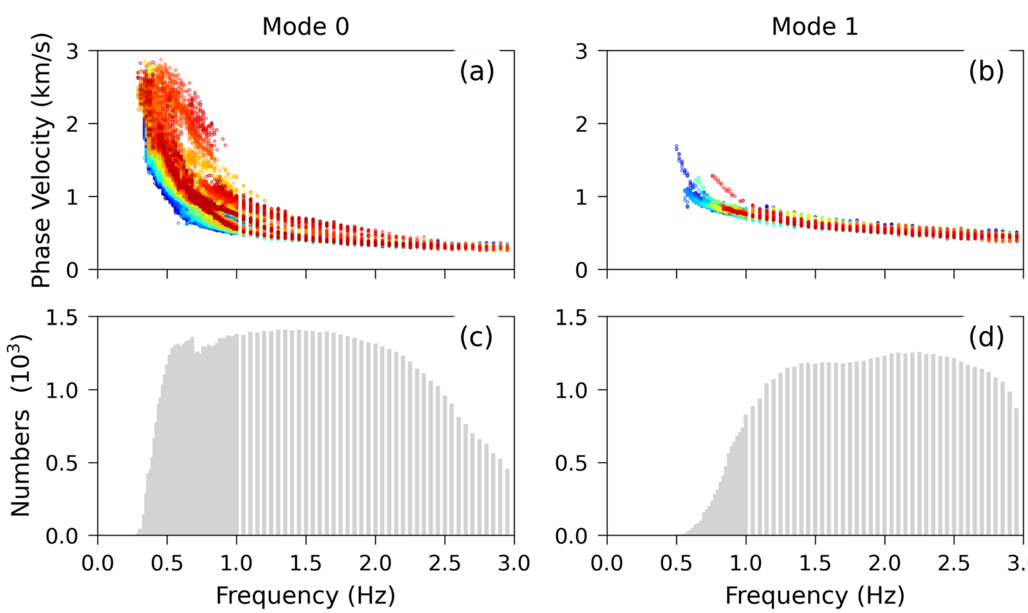

Figure 6. The extracted phase velocities of fundamental mode (mode 0) and the first higher mode (mode 1) as a function of frequency for all subarray. The color represents that is extracted from associated subarray shown in Figure 2b with the same color. (a)The phase velocities for the fundamental mode Rayleigh wave. (b)The phase velocities for the first higher mode. (c) The number of the subarrays in which the effective fundamental mode phase velocities at that frequency can be extracted. (d)The same as (a) but for the first higher mode. The samples in the frequency range of 0.2-1 Hz is large than that of 1.0-3.0 Hz so as to adapt to the larger velocity gradient at lower frequency.

Figure 6 gives the phase velocities of all subarray at different frequency. It shows the effective frequency range of the finally extracted dispersion curves is 0.2-3Hz, which varies with the location of subarray and mode branch. For the fundamental mode, the velocity at frequency range of 0.4-2.5 Hz can be extracted for most subarray. At lower frequency range (<0.3Hz), only for few subarrays the velocity can be extracted with reliable accuracy. As the first higher mode, the dispersion at frequency lower than 0.6 Hz is not available for all subarrays. For most subarray, the available frequency range is 0.8-3 Hz. As we will see from Figure 8 and 9, the subarray where the dispersion is not available usually has a low-velocity thin surficial layer, especially for the first higher mode, the dispersion of which can not be distinguished for almost all subarrays located on the Daxing high for the frequency lower than 1.0 Hz (See Figure 9f). The dispersion of the fundamental mode, however, usually can be extracted for most subarray in the study area. Therefore, both the fundamental mode and the first overtone are used in the inversion as long as they are available. Only the fundamental mode is considered for the subarray where only this mode is available.

4 2-D Phase velocity maps

4.1 Characteristics of phase velocity for different tectonic unit and quality control

Figure 6 shows the extracted dispersion curves have similar trend within a velocity range. The abnormal dispersion curves with extreme high or low velocity, as seen in the dispersion extraction by frequency-time analysis of NCFs in traditional surface wave tomography, were not observed. Therefore, all the extracted dispersion curves are used in the depth inversion once they are available. In fact, we performed the quality control of the dispersion curve when picking them from the beamforming energy.

Quality control and mode recognition is important to ensure the reliability of extracted dispersion curves. Especially, the study area spans different tectonic unit such as sag and high, where Quaternary cover layer with violent varying thicknesses are observed. The characteristics of the fundamental and the first higher mode of surface waves would be affected seriously by such complex varying layered model. And thereby the beamforming output, which indicates the mode branch in f-v domain, would exhibit unique features which would prevent the mode picking from being easily identified.

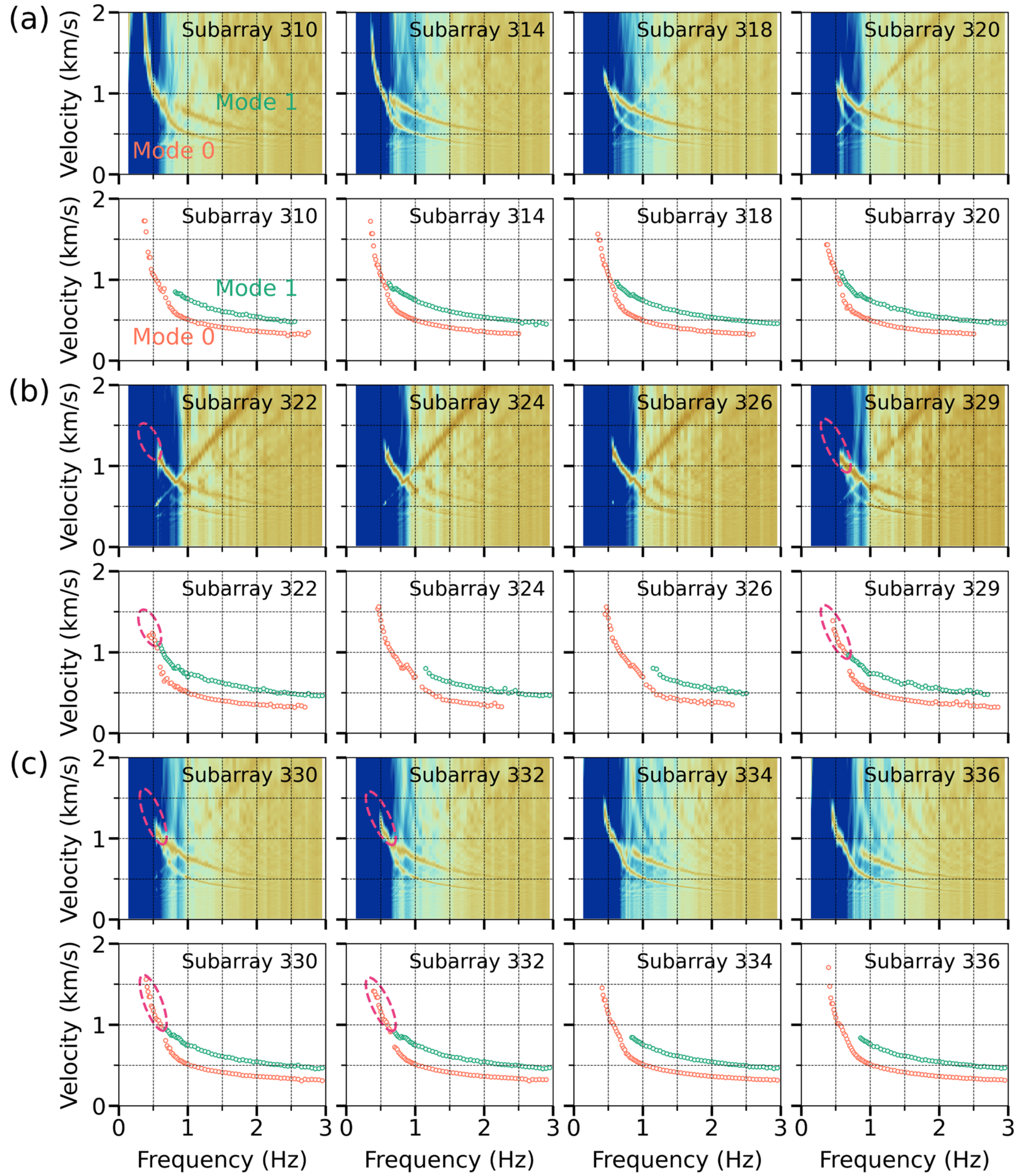

Figure 7 Illustration of the mode identification for the typical subarray located at different tectonic unit. The index of the subarray is labeled in each panel, the location of which are highlighted in Figure 2b and also labeled in Figure 12d, where the S-velocity under them can be seen. The orange and light green circles represent the identified fundamental mode (Mode 0) and the first higher mode (Mode 1), respectively.

As an example, Figure 7 shows the dispersion characteristics for typical subarrays located at different tectonic unit. For each selected subarray, the beamforming energy is given in the top row panels in Figure 8a, 8b and 8c. The identified modes are displayed in the bottom row panels. The fundamental (Mode 0) and the first higher mode (Mode 1) are represented by orange and light green circles, respectively. The location of the subarray labeled in each panel are highlighted in Figure 2b. Although the subarrays 334 and 336, according to the tectonic unit shown in Figure 1b, are located on the DXH, our inverted S-wave velocity model indicates the second tectonic unit named Gangtang sag is developed under these two subarrays (See Figures 12d and 13). Therefore, from number 310 to 336, these subarrays cross the FBS, DXH and Gangtang sag. It can be found from Figure 7, for the subarrays that all involved stations are located on the same tectonic unit such as sag or high, two separated mode branches can be found. For instance, at subarrays 310, 314, 318, which are located on FBS, subarrays 324 and 326, which are located on DXH and subarrays 334 and 336, which are located on Gantang sag, the mode branches are easily to be identified since they are usually separated. The difference is, as expected, the velocity for the subarray at the high is larger than that at the sags. For example, the velocity of the fundamental mode at 1 Hz for subarray 324 and 326 is about equal to 0.7 km/s, is larger than that of the other subarrays, which are usually equal to 0.5 km/s.

For the subarrays located at the transition zone of two tectonic units, that is, involved stations in the subarray crossed both the sag and high area, the mode identification is usually not straightforward due to the mode-kissing. As shown at the bottom vertex of the ellipses in the subarray 322, 329, 330 and 332, the first higher mode intersects with the fundamental one. To avoid the mode misidentification, we determine the mode branch by visual inspection for these cases. A rule of thumb we followed is the priority of the fundamental mode. That is to say, at the low frequency range where only the beamforming energy of one dominant mode is observed, we regard this mode as the fundamental one even the energy at these frequency range seems also to be able to smoothly transition to the first higher mode. As a consequence, the points at low frequency range shown by the orange circles inside the ellipse for such subarrays are recognized as the fundamental mode rather than the first overtone. The length of such frequency range is determined by referring to the beamforming energy of the surrounding subarrays through visual inspection.

Two reasons are responsible for above criteria on mode identification. First, we expect the final model looks more smoother and the abrupt variation at the transition zone between different tectonic units is supposed to be avoided. Take the subarray 332 as an example, dispersion characteristics of its surrounding subarray 334 can obviously identified as the fundamental mode at the frequency below 0.8 Hz. Considering this feature, the frequency range marked in the ellipse for subarray 332 is also recognized as the fundamental mode even it has a quite succession with the first higher mode, and moreover only one mode is observed at these frequency range. Secondly, for dispersion extraction using the frequency-time analysis based on the NCFs, the dispersion located this frequency range is normally recognized as the fundamental mode if only one mode is dominant. As shown by the imaging results, this criteria for mode identification is proved to be reliable.

4.2 Phase velocity maps

The lateral variation of the phase velocity at each frequency can then be obtained without tomographic inversion by mapping the available azimuth-averaged phase velocity of subarrays to their reference point. Figure 8 shows the 2D phase velocity maps of the fundamental mode Rayleigh wave at 9 selected frequencies. The results of the first higher mode is given in Figure 9 at 6 selected frequencies. The subarrays where the velocity is not available are left blank in the panels.

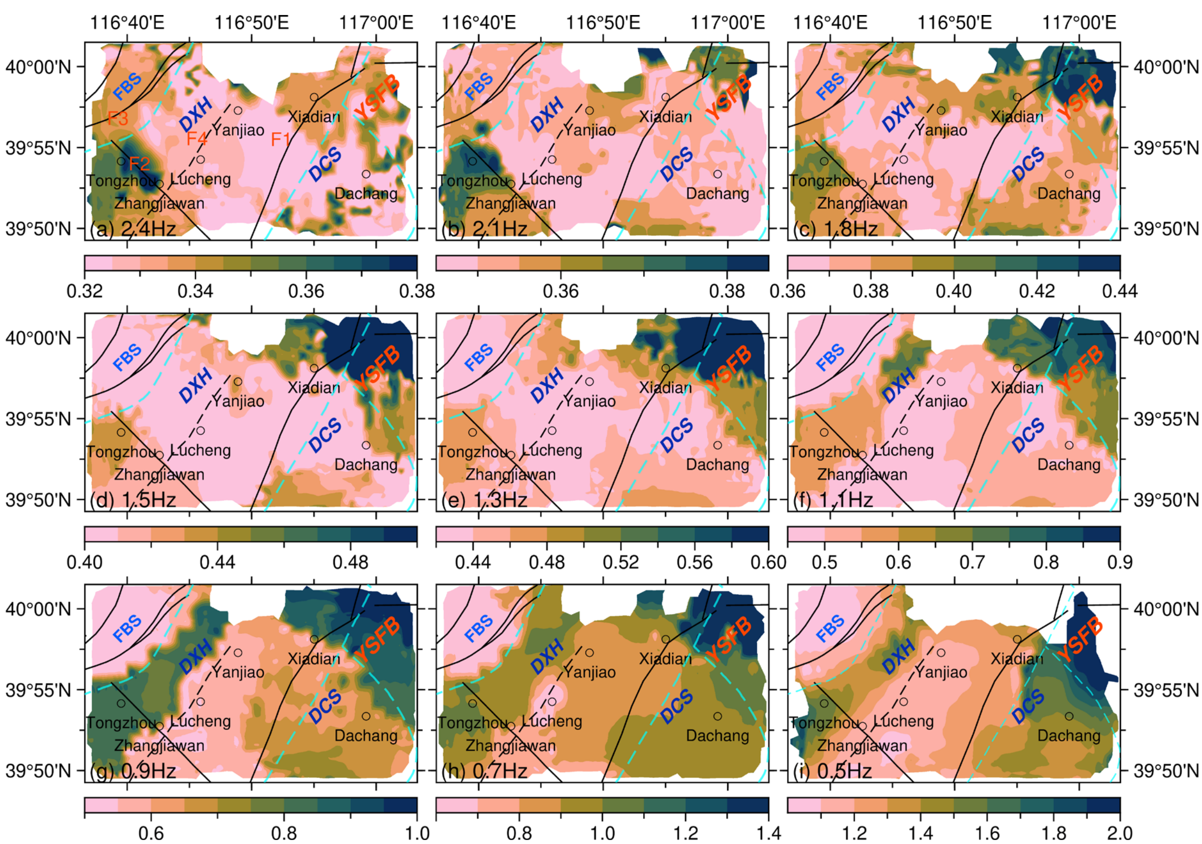

Figure 8. 2D phase velocity maps of the fundamental mode Rayleigh wave at 9 selected frequencies. The faults are denoted by black solid lines. F1: Xiadian Fault; F2: Nankou-Sunhe Fault; F3: Nanyun-Tongxian Fault; F4:

Northeast extension of Daxing fault, inferred from our model, is denoted by black dashed line. FBS: Fengbo Sag; DCS: Dachang Sag; DXH: Daxing High; YSFB: Yanshan Fold Belt. Aqua dashed line denotes the boundary of the tectonic units.

It can be seen from Figure 8 the velocity of the fundamental mode Rayleigh wave is available at 0.5-2.4 Hz for most subarrays except some subarrays located around north and northeast of the study area. At these areas, the results are not available either for the first higher mode shown in Figure 9 for frequencies higher than 1.3 Hz. For the frequency of 1.1 Hz or lower, besides these areas, it is even not available for the first higher mode at the area along the DXH where a high velocity is supposed to be observed for this frequency range. Hence only the results at frequency range of 1.1-2.4 Hz are shown in Figure 9.

In general, Figure 8 shows the lateral variation of the phase velocity agree well with the tectonic units. For the shallow structure, usually reflected by the velocity at higher frequency (>1.1 Hz), two fast anomalies appear in the southwest and northeast of the study area, corresponding to the DXH and YSFB, respectively. Low velocities are observed at the northwest and southeast of the study area, which agree well with the location of the FBS and DCS, respectively. For the structure at deeper reflected by the velocity at frequency of 1.1 Hz or lower, from northwest to southeast, the bandlike pattern of the velocity variation along NE orientation can be observed which is consistent with the tectonic strike. At the northwest corner, FBS presents low velocity anomaly. In the northwest of the Daxing fault (F4), DXH shows obvious high-velocity anomaly. However, it shows low-velocity anomaly at the area between the Daxing and Xiadian fault. We infer the second tectonic unit such as sags are developed in this area, as we will see in section 5.3. Continue to southeast, we enter DCS and YSFB. YSFB present high-velocity, as expected. The mid-velocity is observed at DCS, which implies the thickness of the sedimentary deposits in DCS is probably thinner than that in FBS.

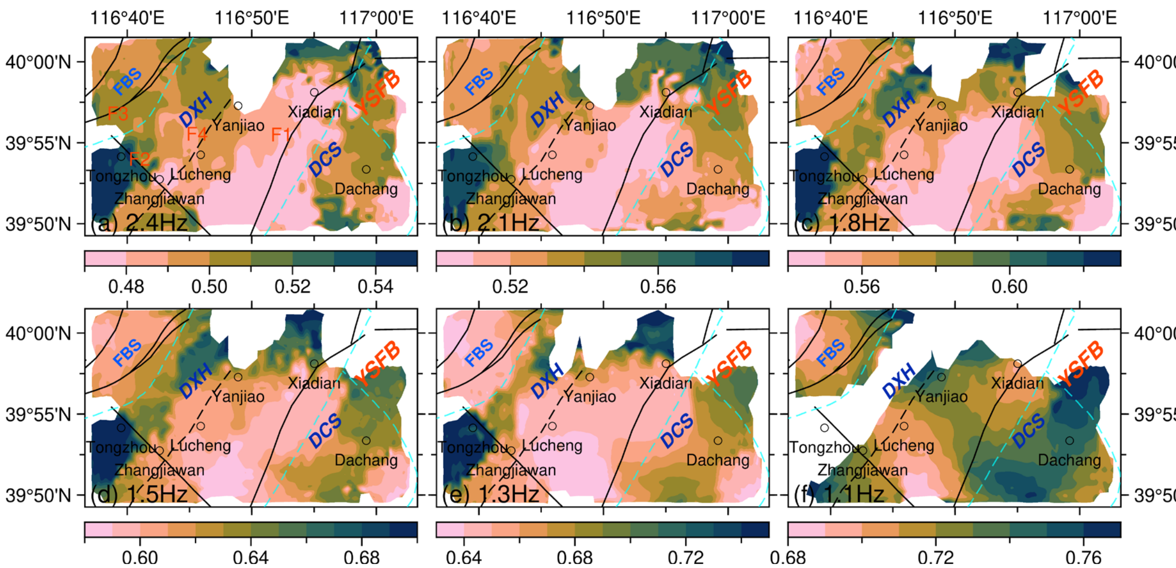

Figure 9. 2D phase velocity maps of the first higher mode of Rayleigh wave at 6 selected frequencies.

As the first higher mode, the lateral variation is similar as that for the fundamental mode but with a higher velocity and shift frequency, as expected. For example, the velocity variation of the first higher mode at frequency range of 1.1-2.4 Hz resemble with that of the fundamental mode at frequency range of 0.5-1.1 Hz. The fact that the phase velocity of the first higher mode is more sensitive to deeper structure than that of the fundamental mode can be illustrated by comparing Figure 9 and Figure 8. The appearance of DXH with high velocity can be distinguished from the frequency of 1.1 Hz or lower for the fundamental mode, but it can be observed clearly at frequency of 2.1 Hz in Figure 10 for the first higher mode.

Considering the velocity variation shown in Figure 8 and 9, it can be reasonably speculated that the velocity at those areas without available results is relatively high and implies a thinner low-velocity cover layer. We therefore concluded that it is usually more difficult to extract the dispersion curves for the structure with thin low-velocity overburdens, at least for current basin structure of Tongzhou.

5 3-D S-wave Velocity Model and Tectonic Implications

5.1 Depth Inversion

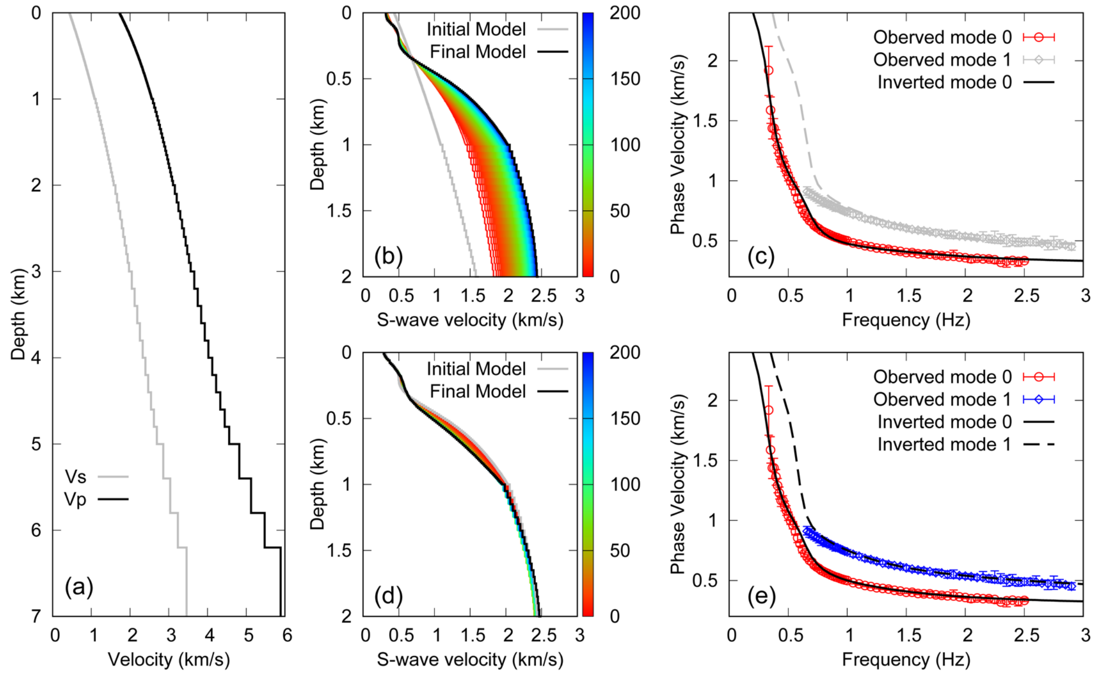

Figure 10. Initial model and the depth inversion. (a)The initial velocity model for P-wave (Vp) and S-wave (Vs). (b)The variation of the inverted S-wave velocity model with iterations for the case only fundamental mode is considered in the inversion. The black solid line denotes the final model. (c)The fitting of the predicted phase velocity of the final model with the observed one. Only the fundamental mode shown by the red circles is used in the inversion. (d) The same as (a) but the observed data of two modes are considered in the inversion. The initial model denoted by solid gray line is the final one shown by the solid black line in (a). (e)The same as (c) but observed data of two modes are used in the inversion.

For all subarrays where the dispersion curves are available, the 1D velocity profiles at each reference point can be obtained by fitting the dispersion curves via the depth inversion. We use the program developed by Herrmann (2013) to invert for the S-wave velocity, where a linear algorithm is designed to minimize the difference between the observed velocity and the one of the predicted models. The choice of the initial model would affect the convergence and stability of the inversion. To make the initial S-wave velocity model, we first take the average of the observed velocity of the fundamental mode. The wavelength-velocity relation is then calculated using the averaged dispersion curve. By multiplying the phase velocity with 1.5, the modified wavelength-velocity is taken as the initial S-wave depth-velocity model. The velocity at the bottom half space is taken as 3.46 km/s, i.e., the averag S-wave velocity of 0-20 km for the 1D global velocity reference model.

Only the S-wave velocity is inverted. P-wave velocity is calculated using its relation to S-wave given by Brocher (2005). Figure 10a shows the initial model of S- and P-wave velocity which has a varying sampling with depth. A constant initial density, 2.1 g/cm^3, is taken for all depth by referring the result of Peng et al (2020). For each iteration, the Poisson's ratio, which is calculated by initial S- and P-wave velocity, keep fixed. P-wave velocity is updated according to the Poisson's ratio and the inverted S-wave velocity. The density is then updated from P-wave velocity, based on the Nafe-Drake relation which expressed the density as a function of P-wave velocity (Nafe & Drake,1963; Brocher, 2005).

When performing the depth inversion, only the fundamental mode is used if the dispersion curve of the first higher mode is not available. Both of them are considered in the inversion once they are all available for the subarray. For the latter case, the model obtained using only the fundamental mode is taken as the new initial model and the final model is then determined by fitting the dispersion curves of two modes. The inversion procedure is illustrated in Figure 10, where the velocity under the subarray of 230 are inverted. Figure 10b shows the evolution of the model with iteration for the inversion of the fundamental mode. We take the model after 200 iterations as the final one, which is shown by the black solid line in Figure 10b. The inverted results were stable and tend to converge after 100 iterations. Figure 10c shows the dispersion curves of the predicted model and the observed one. It can be seen the precicted first higher mode at frequency of 0.6-1.0 Hz does not fit well with the observed one. Model evolution for the inversion using two modes is given in Figure 10d. Although the model variation is not as impressive as shown in Figure 10b, the adjustment of the model at depth of 0.2-1 km can still be clearly seen in Figure 10d, which improved the fitting of the first higher mode at frequency of 0.6-1.0 Hz, as shown in Figure 10e.

We checked the inversion schemes described above for subarrays with different location. The final model can generally be determined with pretty convergence and stability. As shown in Figure 10, although the depth of the initial model is given up to 7 km, only the results at 0-1 km depth are selected to discuss based on sensitivity analysis. The sensitivity of the phase velocity with respect to the S-wave velocity of two typical predicted model is given in Figure 11. It is plotted as the function of depth and frequency. Only the results at frequencies where the observed data is available are shown. The predicted model is the structure under the subarray 230 (Figures 11a and 11b) and 1220 (Figures 11c and 11d), which are framed by a box in Figure 2a.

Figure 11 shows the phase velocity of the fundamental mode is mainly sensitive to the depth of 0-0.5 km for the available frequency range. For the first higher mode, the significant sensitivity to the depth up to 2 km can be observed for frequencies lower than 1 Hz. However, only the results at 0-1.0 km depth are selected to discuss for safety.

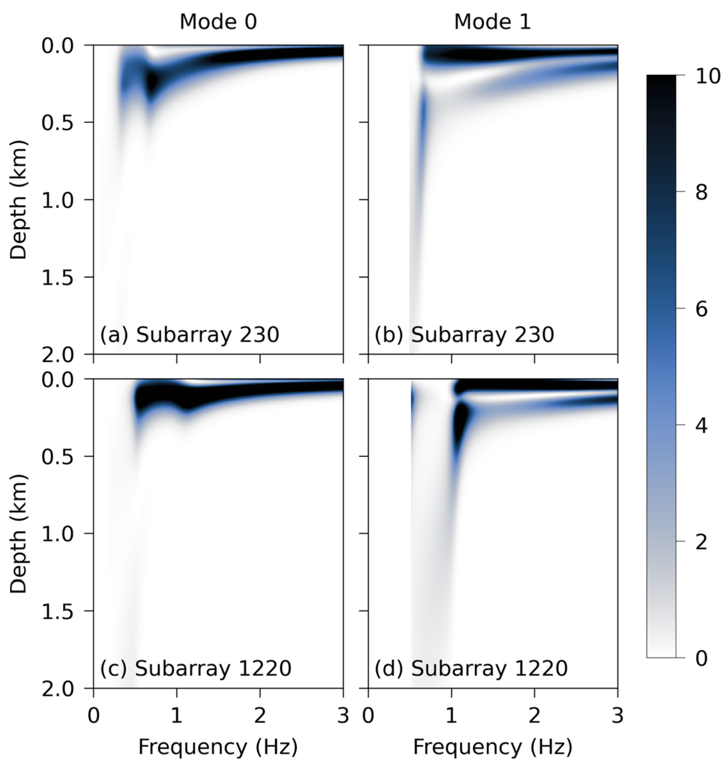

Figure 11. The sensitivity kernel of the phase velocity with respect to the S-wave velocity. It is plotted as the function of the depth and frequency. Only the results for available observation frequencies are shown. (a) The sensitivity of the fundamental mode (labeled by mode 0) of the predicted model under the subarray of 230. (b)The same as (a) but for the first higher mode (labeled by mode 1). (c) and (d) are respectively the same as that shown in (a) and (b) but for the predicted model under the subarray of 1220.

5.2 Characteristics of the S-Wave Velocity Model

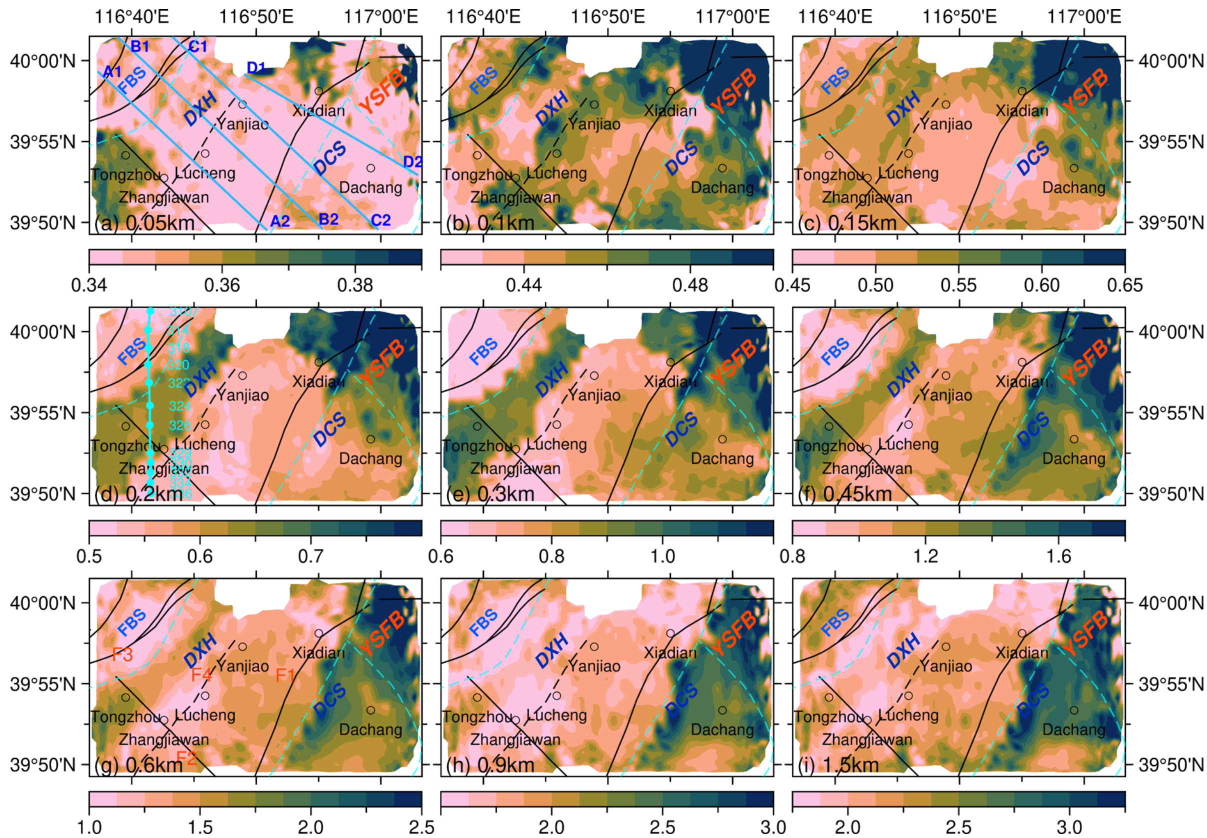

Figure 12. The S-wave velocity at depths of 50 m, 100 m, 150 m, 200 m, 300 m, 450 m, 600 m, 900 m and 1.5 km. The results are obtained by cubic interpolation based on the velocity at each depth of the available subarray. The subarrays where the reliable results are not available, mainly located on the edge and the north of the study area, are left blank in the panels. The cross sections A1-A2, B1-B2, C1-C2 and D1-D2 are discussed in Section 5.3 and 5.4. The illustration of the dispersion extraction for the subarrays labeled in (d) is shown in Figure 7.

Combining the 1D velocity profiles of each reference point and performing 2D cubic interpolation for each depth, we finally produce a 3D S-wave velocity model. Figure 12 shows the inverted S-wave velocity at depths of 50 m, 100 m, 150 m, 200 m, 300 m, 450 m, 600 m, 900 m and 1.5 km.

From a tectonic point of view, as shown by Figure 2b, the study area crosses four tectonic units. From the northwest to southeast, we observe FBS, DXH and DCS. The northeast of the study area is supposed to enter the YSFB.

At 50 m depth, since the study area is covered by the Quaternary deposits, the S-wave velocity is usually lower than 350 m/s and the lateral variation of the velocity is not significant except the southwest where relatively high velocity is observed. It is supposed to be the effect of DXH.

With increasing depth, the lateral variation of the velocity is gradually becoming more obvious. At depth 100-150 m, significant high velocity of more than 600 m/s can be observed at the northeast of the study area. This high velocity region is located in the YSFB. Further to the northeast, outside the study area, the bedrock is outcropping. Previous results show the covering Quaternary sediments at this region is fairly thin. For the same reason and considering the continuity of lateral variation, it is reasonable to speculate that a quite higher velocity would also be observed at the north part of study area due to the presence of metamorphic rock and granite close exposed at that region, even where the results are not available (It can be seen from the topography shown in Figure S1 in the supporting information, in the north part of the study area the altitude is relatively high).

At 200-600 m depth, it still shows the high-velocity anomaly in YSFB. The low velocity anomaly varying from 500 m/s to 1 km/s is observed at FBS. Adjacent to FBS, DXH are obviously characterized by a high-velocity belt with NE-striking varying from 650 m/s at 200 m depth, to 1650 m/s at 600 m depth. The transition zone, from low velocity at FBS to the high velocity at DXH, coincides with the boundary of the tectonic units indicated by aqua dashed line. See continue to southeast, the low-velocity feature can be observed between Daxing fault and Xiadian fault, which is probably a manifestation of the development of second-order tectonic unit such as sags in DXH. To the southeast corner, at DCS, we observe a mid-velocity feature. This suggests the thickness of the sedimentary layer is probably thinner in DCS than that in the area around Xiadian and Zhangjiawan, where two sags are observed. This will be discussed in section 5.3.

At depth more than 600 m, the high-velocity at the location of DXH disappear. Maps are similar except for a general slight increase of the average velocity with depth. Bounded by Xiadian fault, a notable low-velocity is observed at the northwest, while at the southeast it shows a high-velocity anomaly. This feature for lateral variation is maintained up to a depth of 2 km just with an increasing average velocity. At the southeast corner, below the Dachang, the velocity is relatively lower than that in YSFB, as expected. The results at 1-2 km depth will not be discussed due to the limited sensitivity of the phase velocity at this depth range, as shown in Figure 11.

5.3 Thickness of Sedimentary Deposits

The earthquake disaster is mainly caused by strong ground motion on the surface, which depends on the seismic wave velocity, attenuation, and density of an area under the surface. The S-wave velocity and the spread of the basement depth are particularly important since, for example, the area within the basin composed of poorly consolidated sediments with low S-wave velocity generally experiences greater shaking intensity and duration than the ground outside the basin composed of bedrock.

The obvious interface indicating the thickness of the sediments is not included in the 3D S-wave velocity model inverted from the surface wave dispersion. Because the phase velocity is not sensitive to the interface and we make the initial model composed of many thin layers without obvious boundary of impedance contrast, the S-wave velocity profile at each subarray is thereby a curve with continuous variation. As an alternative, we select the isosurface of S-wave velocity at a given value as the possible thickness of sedimentary layer. The value is estimated as 1 km/s by calibrating it with the thickness of Quaternary sediments measured from the drilling data. The data from three boreholes labeled by ZK07, ZK08 and ZK10 in Figure 1b are used in calibration. The depth to the bedrock from these boreholes is given in Table 1, which are taken from Lei et al.(2021).

Figure13a shows the isosurface of S-wave velocity at 1 km/s. Generally speaking, it agrees well with the tectonic units. The depth of the isosurface in FBS at the northwest of the study area is 400-600 m. In addition, the other two regions with 400-600 m isosurface depth were observed around Gantang and Xiadian. The deepest location can reach 700 meters. Except these three sags, the depth of the isosurface at DXH and YSFB is relatively shallow, usually about 200-500 m. It is worth noting in the northern part of the study area, directly above Yanjiao, the effective dispersion curve cannot be extracted using beamforming analysis, and thereby the S-wave velocity is not available. This may be related to the extremely thinner deposits.

Table 1 The depth to the bedrock obtained from three methods*

Boreholes	Depth to the Bedrock (m)	Isodepth at 1 km/s (m)	Thickness from H/V (m)
ZK07	315	366	323

ZK08	478	488	339
ZK10	318	319	306

* The data of the boreholes is taken from Lei et al.(2021)

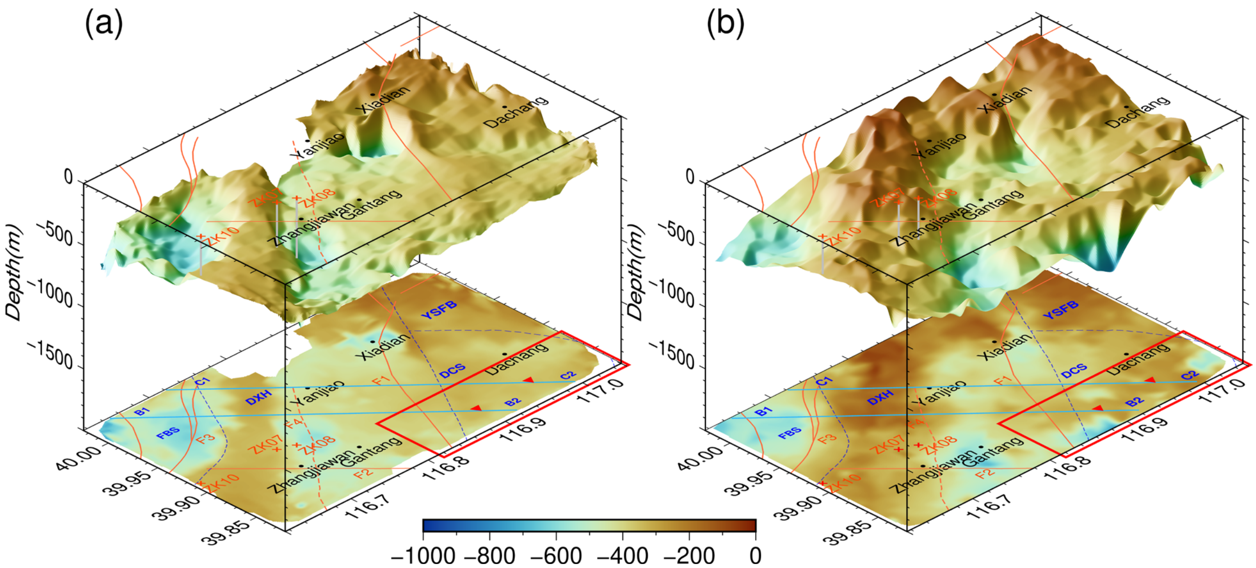

Figure 13. The isosurface of S-wave velocity at Vs = 1 km/s (a) and the thickness of the sediments obtained by H/V spectral ratio (b). Northeast extension of Daxing fault (F4), inferred from our model, is denoted by orange dashed line. Blue dashed line denotes the boundary of the tectonic units. The area where the thickness inferred from two methods has much difference is marked by red box. Two cross sections along lines B1-B2 and C1-C2 are given in Figure 14. The H/V curves at two stations denoted by red triangles are given in Figure S4 in the supporting information.

On the other hand, the definition on the thickness of the sedimentary layer may vary at different locales used for different field (Shah & Boyd, 2018). If unconsolidated sediments layer directly covers the igneous or metamorphic rock, it is straightforward to define the unconsolidated sediments as the thickness of the sedimentary layer. If the sediments gradually consolidate with depth, it is difficult to define the sedimentary layer and the depth to the bedrock, especially only the S-wave velocity is available since it has probably the similar value for the consolidated sediments as the bedrock. Therefore, in order to verify the results given by the isosurface of S-wave velocity, we also use the H/V spectral ratio to delineate the depth to the basement.

We calculate the spectral ratio $HV(f)$ of the horizontal to vertical component by

$$HV(f) = \frac{H(f)}{Z(f)} = \frac{\sqrt{N^2(f) + E^2(f)}}{Z(f)} \quad (2)$$

Where, $N(f), E(f)$ and $Z(f)$ are respectively the Fourier spectrum of the continuous records of North, East and Vertical component. We calculate the Fourier spectrum using the raw data with 200 Hz sampling and divide the continuous record into 900s segments with 450s overlap. The final spectrum of each component is then obtained by averaging the Fourier spectrum of each segment and the $HV(f)$ is then calculated by equation (2).

The fundamental resonance frequency f_0 is identified by picking the frequency associated to the maximum pick of $HV(f)$ at the frequency range of interest (See Figure S2 and S3 in the supporting information for the H/V spectral ratio at typical subarray located at different tectonic unit). The thickness h of the sediments is then estimated through the following empirical relation (Ibs-von Seht & Wohlenberg, 1999; D'Amico et al., 2008)

$$h = af_0^b \quad (3)$$

Where a and b are coefficients, which is usually determined by calibration using the priori information of the study area. We take $a = 103.2, b = -1.251$ by referring Peng et al.,(2020), where they study the thickness of the sediments of a larger range around our study area using the similar method but with a much sparse array (See Figure S3 in supporting information for the H/V spectral ratio after transferring the frequency to the depth for the subarray located at different tectonic unit).

The final result on the thickness of the sediments in the study area is given in Figure 13b. It can be found from Figure 13 the isosurface of S-wave velocity at 1 km/s has a high correlation with sedimentary thickness obtained by H/V spectral ratio. FBS, and two sags around Gantang and Xiadian can be obviously seen for both of the methods, with similar thickness about 400-600 m. At DXH and the northeast area near YSFB, the thickness given by H/V is about 100-400 m, 100 m shallower than that suggested by the isosurface of S-wave velocity at 1 km/s. At the north of the study area, where the results from isosurface is not available, the thickness given by H/V spectral ratio is about 50-100 m. This verified our conjecture that the area without available dispersion is usually covered by an ultra-thin sedimentary layer.

As shown in Table 1, the depth of the isosurface at the location of boreholes ZK07 and ZK10 are respectively 366 and 319 m. The depth to the basement given by H/V ratio respectively is 323 and 306 m. These estimates are in good agreement with the results directly seen from drilling, which are respectively 315 and 318 m. As the borehole ZK08, the depth of the isosurface of S-wave velocity at 1 km/s is 488 m, which is similar as that given by drilling, 478 m. The result given by H/V method is 339 m, which underestimates the actual measurements. This is probably related to ZK08 being in the transition zone between DXH and Gantang sag, where the thickness of the sedimentary layer usually has a variation with large gradient. The assumption of the layered model for single-station H/V technique may not be valid. Although this is also an assumption for beamforming, the average effect over the inter-station involved in the subarray may relax the requirements of this assumption.

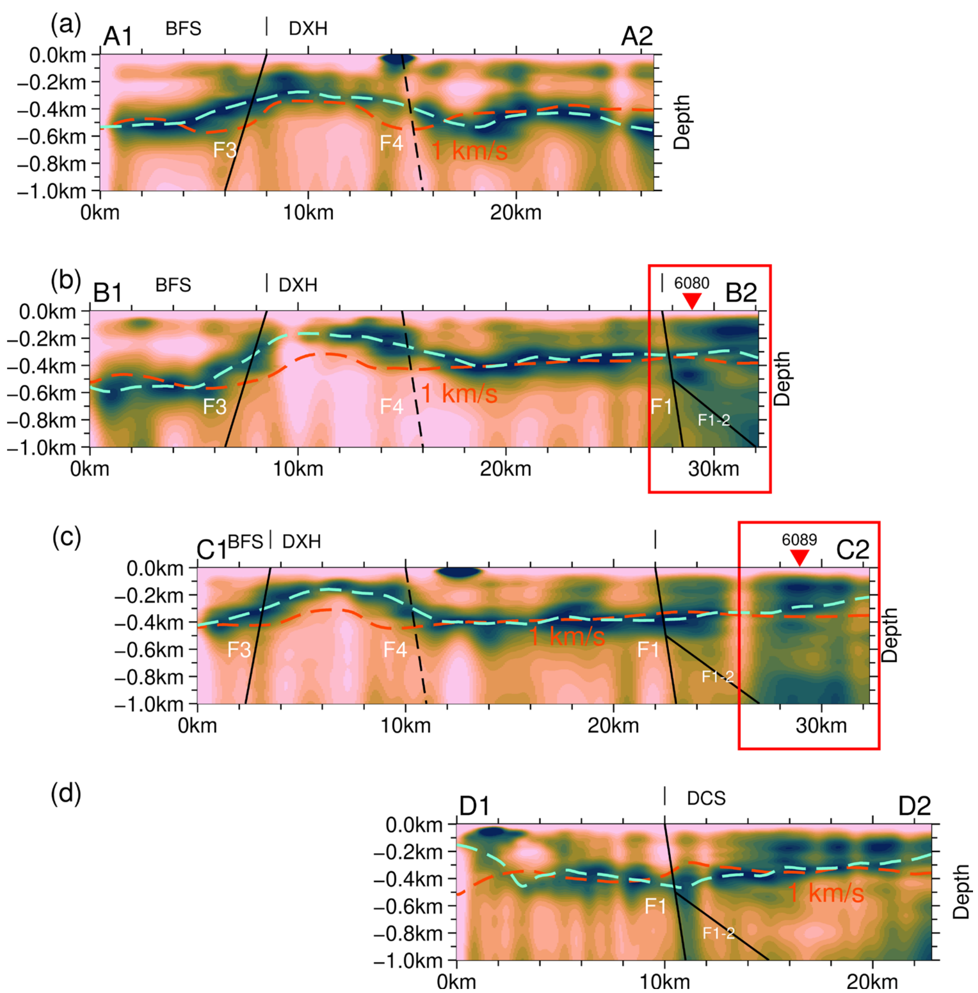

Figure 14. Cross sections of the sedimentary thickness delineated by H/V spectral ratio along lines A1-A2, B1-B2, C1-C2, and D1-D2, which are marked in Figure 1b. The location of the faults is indicated by the thick

black line. F1: Xiadian Fault; F3: Nanyuan-tongxian Fault; F4: predicted location of the extension of Daxing Fault. The H/V curves at two stations denoted by red triangles in (b) and (c) are given in Figure S4 in the supporting information.

In the south edge of the study area, especially at the southeast area marked by red box where it is supposed to be the northern end of the DCS, the thickness given by H/V spectral ratio has large lateral variation. The deepest is up to 700 m. The thickness given by the isosurface of S-wave velocity at 1 km/s is about 300-400 m. Two possible reasons can explain the difference given by H/V and isosurface of S-wave velocity. Firstly, this is probably related to the beamforming method with moving subarray. The aperture of the subarray is about 10 km. The results given by beamforming is the average over the stations inside the subarray which spread the area with different sedimentary thickness. While the results estimated by H/V spectral ratio is determined by the data of single station without averaging. This could explain the lateral variation is relatively smooth for the results given by isosurface of S-wave velocity.

Another reason is related to H/V technique. The sedimentary thickness is estimated from the resonance frequency of H/V curve. It requires the resonance frequency or equivalently the transferred sedimentary thickness can be distinguished from H/V curve. However, in the area marked by red box in Figure 13, it is difficult to distinguish the resonance frequency of H/V curve. This means there is possibly no obvious interface with strong impedance contrast in this area. To explore this issue, 4 cross sections of the H/V spectral ratio along lines A1-A2, B1-B2, C1-C2 and D1-D2 depicted in Figure 1b are given in Figure 14(See Figure S3 in the supporting information for plotting such cross section along a given line). The red dashed line denotes the isodepth of the S-wave velocity at 1 km/s. The aqua dashed line denotes the sedimentary thickness picked from the maximum of H/V spectral ratio. As mentioned above, except for DXH where the thickness given by H/V is slightly shallow, the thickness indicated by two dashed lines is highly correlated. At most locations, the maximum of H/V spectral ratio can be clearly distinguished. However, we found in the area marked in the red box in cross sections B1-B2 and C1-C2, it is difficult to determine the thickness by picking the maximum, since the dark green, which indicates the larger amplitude of H/V spectral ratio, almost spread the whole depth range. In this area, based on prior information, we select visually the thickness corresponding to the peak frequency at the mid position rather than the frequency with maximum which usually gives an extreme shallow or extreme deep thickness(See Figure S4 in the supporting information for

H/V curves at two stations denoted by red triangles in Figure 14b and 14c). Even so, the thickness given by H/V still has a large lateral variation. On the contrary, the lateral variation for the results given by the isodepth of S-wve velocity is relatively smooth and is more consistent with the isopach of Quaternary sediments shown in Figure 1b. This also gives us an inspiration, extra attention should be paid in some area when applying the H/V technique to extract the thickness of the sediments.

On the other hand, it should be pointed out that the depth given by the isosurface of S-wave velocity or by the resonance frequency of H/V spectral ratio cannot be regarded as the strictly defined thickness of sedimentary deposits or the Quaternary sediments. They are the impedance interface with strong contrast which is usually related to the velocity difference. Nevertheless, the combination of inversion with multi-mode surface wave and the H/V method proposed in this paper present an estimation on the thickness of the sedimentary deposits with fairly reliability.

5.4 Northeast Extension of Daxing Fault

As shown in Figure 1a, it is generally believed the north section of the Daxing fault refers to the section between Tongbai fault (F7) and Niubaotun, with a length of about 10 km, forming the boundary between DXH and LGS. It connects with Xiadian fault via NW-striking Niubaotun fault. Xiadian fault is thought as the boundary between DXH and DCS. However, the detection results from the petroleum and geological community suggest the sign of the connecting fault with NW-striking is not obvious, or at least the extension of the fault is not enough to cut the Daxing and Xiadian fault.

The results from seismic reflections show (He et al., 2020) the Daxing fault continues to extend along NNE direction after passing through Niubaotun. The extension is about 13 km long, parallel to Xiadian fault. Our 3D S-wave velocity model and features of the impedance interface delineated by H/V seems to supporting this, i.e., the Daxing fault probably extends towards to NNE direction rather than ending at Niubaotun.

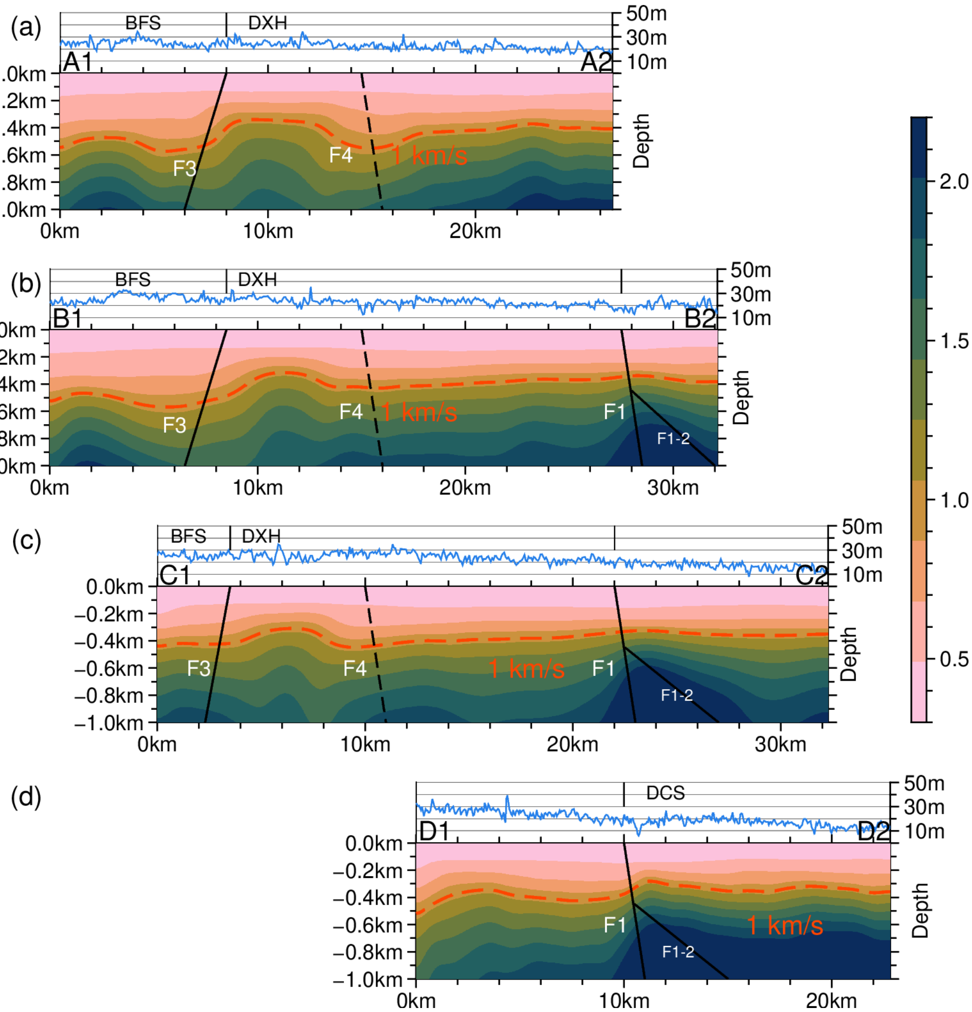

Figure 15. Cross-sections of S-wave velocity along lines A1-A2, B1-B2, C1-C2 and D1-D2, which are marked in Figure 1b. The isoline of 1 km/s are indicated by the red dashed line. The location of the faults are denoted by the black line. F1: Xiadian Fault; F3: Nanyuan-tongxian Fault; F4: predicted location of the extension of Daxing Fault.

To explore the NE extension of Daxing fault, 4 cross sections of the S-wave velocity along lines A1-A2, B1-B2, C1-C2 and D1-D2 shown in Figure 1b, which is nearly perpendicular to NE-striking faults, are given in Figure 15. For sections A1-A2, B1-B2 and C1-C2, we align them at Nanyuan-Tongxian fault (F3). Section D1-D2 is aligned with section C1-C2 at Xiadian fault (F1). The red dotted line in the figure indicates the isodepth at 1 km/s. The location of the known faults such as Nanyuan-Tongxian fault (F3) and Xiadian fault (F1) are marked with black solid lines. The results from deep seismic sounding show (Liu et al, 2009; Liu et al, 2011) that there are two faults with SE-dipping at the location of Xiadian fault, namely F1 and F1-2 shown in Figure 15. F1 is a relative new fault that possibly cut the Moho. F1-2 is a listric fault that was cut by F1 at 450 m depth, as shown in Figure 15. The predicted location of the NE extension of Daxing fault (F4) is represented by black dashed line.

From northwest to southeast, sections A1-A2, B1-B2, and C1-C2 pass through FBS, Nanyuan-Tongxian fault (F3), DXH, Gantang sag, and finally cross the Xiadian fault (F1). The isodepth of 1 km/s at FBS, DXH and Gantang sag, are 400-600m, 200-500m, and 400-600m, respectively. The S-wave velocity at DXH is significantly larger than that on both sides of it, showing obvious tectonic characteristics of the anticline, which probably indicates the dislocation of the strata on both sides of DXH. At the southeast side of DXH, the position where the S-wave velocity with larger lateral variation, we deduce it is the northeast extension of Daxing Fault, as shown by the black dashed line with label F4 in Figure 15a, 15b, and 15c.

Meanwhile, at predicted positions the sign on the dislocation of the impendence interface given by H/V can also be observed. It can be found in Figure 14b and 14c, two peaks can be found near the position shown by the balck dashed line, which we think it is a sign on strata dislocation. Moreover, this characteristic on the dislocation is similar as that on the other side of DXH at the position of the balck solid line labeled F3, which is the position of the known Nanyuan-Tongxian fault.

Combining previous results from seismic reflections (He et al., 2020) and gravity anomaly in the study area (Lei et al, 2021), we therefore deduce Daxing fault continues to extend northeast after passing through Niubaotun. The extension length is up to 20km, reaching the northern part of the study area, where a thin sediments is suggested by H/V and our 3D S-wave velocity model is not available. In Figure 13, we also present the predicted location of the northeast extension of Daxing fault (F4). It can be seen bounded as Daxing fault, DXH has a relatively shallow sedimentary thickness in the northwest of Daxing fault. Gantang and Xiadian sags are mainly developed on the southeast of Daxing fault, where a relatively deeper sedimentary thickness can be observed.

6 Conclusions

Rayleigh wave phase velocity maps at frequencies between 0.3 and 2.5Hz for the fundamental mode, as well as 0.8 and 3.0 Hz for the first high mode are obtained in the area of Tongzhou, the subcenter of Beijing. The 3D S-wave velocity model of this area is then established with lateral resolution of 1km by depth inversion using the dispersion curves of these two modes at all available subarrays. The thickness of the sediments, which is delineated by the interface with strong impedance contrast obtained by microtremor H/V spectral ratio, is included in the model.

The model agrees pretty well with the characteristics of the tectonic units in the study area. Three sags with 400-600m thickness of the sedimentary deposits are observed clearly. The thickness of the sediments at DXH is about 100-400m. The model implies the Daxing fault possibly continue extends northward. The extension length is up to 20 km.

From the viewpoint of the observation and imaging, dense array at different scales and imaging technique based on seismic noise are two breakthroughs in seismology in the past few decades. The beamforming with moving subarray fully explored these two advances. Based on the dense array consist of more than 900 stations, it was proved in this paper the lateral variation of the phase velocity of multi-mode surface waves can be obtained with sufficient accuracy by beamforming the seismic noise with moving subarray without tomography. The 3D S-wave velocity model with high resolution can therefore be established by depth inversion of multi-mode surface wave inversion. Compared with traditional two-step surface wave inversion based on NCFs, the advantages of beamforming lie in: 1) The creation of 2D phase velocity is straightforward. It does not require pure path inversion and thus the selection of dispersion curve is avoided, which is usually a cumbersome task. 2) As long as the azimuthal anisotropy is not a concern, it does not depend on the distribution of noise source and array geometry. 3)A robust velocity estimation can be obtained since the velocity under the subarray only depends on the data from the stations located inside this subarray.

As a local method, the main drawback is the lateral resolution is not high for long period since a subarray with larger aperture is needed for dispersion extraction with enough accuracy. This could be mitigated by using the subarray with varying aperture suitable for the period range of interest. As a result, the multi-scale imaging with varying lateral resolution at different depth can be achieved.

In addition, if the seismic noise is dominated by more than one mode, due to the possibility of mode misidentification, it is difficult to extract the reliable dispersion using the traditional frequency-time analysis method based on NCFs of inter-station. For this case, it may be essential to consider the array technique such as the beamforming to extract the multi-mode dispersion curves. The successful application in Tongzhou area convinced us the beamforming with moving subarray, combined with the technique of microtremor H/V spectral ratio, can find its potential application in oil and gas investigation, as well as the high-resolution imaging in fault zones and urban area, where usually more than one surface mode is dominant due to the complex near-surface structure.

Acknowledgments

3D S-wave velocity model are openly available from the figshare.com (doi: 10.6084/m9.figshare.17012945). This work was supported by the National Natural Science Foundation of China (U1839209) and the National Key R & D Program of China (2017YFC1500200). The discussion on the distribution of faults and sedimentary thickness benefited from talking with Zhengqin He and and Wenbin Chen.

References

Aki, K.(1957). Space and time spectra of stationary stochastic waves with special reference to microtremors. *Bulletin of the Earthquake Research Institute*, **35**:415-456.

Arai, H., & Tokimatsu, K.(2004). S-wave velocity profiling by inversion of microtremor H/V spectrum. *Bulletin of the Seismological Society of America*, 94(1): 53-63.

Ben-Menahem, A. & Singh, S. J.(1968). Multipolar elastic fields in a layered half space. *Bulletin of the Seismological Society of America*, 58 (5): 1519–1572

Bensen, G., Ritzwoller, M., Barmin, M., Levshin, A., Lin, F., Moschetti, M., Shapiro, N.M. & Yang, Y.(2007). Processing seismic ambient noise data to obtain reliable broad-band surface wave dispersion measurements. *Geophysical Journal International*, 169(3), 1239–1260.

Brocher, T.M.(2005). Empirical Relations between Elastic Wavespeeds and Density in the Earth's Crust. *Bulletin of the Seismological Society of America*, 95(6), 2081–2092. https://doi.org/10.1785/0120050077

Campillo, M. & Paul, A.(2003). Long-range correlations in the diffuse seismic coda, *Science*, 299:547.

Chen, X.(1999). Seismogram synthesis in multi-layered half-space Part I. Theoretical formulations. *Earthquake Research in China* (in Chinese), 13(2),149-174

Chávez-García, F.J., & Luzón, F.(2005). On the correlation of seismic microtremors. *Journal of Geophysical Research: Solid Earth*, 110, B11313,doi:10.1029/2005JB003671.

Chávez-García, F. J., Rodriguez, M., Stephenson, W.(2006). Subsoil structure using SPAC measurements along a line. *Bulletin of the Seismological Society of America*, 96(2): 729-736.doi: 10.1785/0120050141

Chmiel, M., Mordret, A., Boué, P., Brenguier, F., Lecocq, T., Courbis, R., Hollis, D., Campman, X., Romijn, R. & Van der Veen,W.(2019). Ambient noise multimode Rayleigh and Love wave tomography to determine the shear velocity structure above the Groningengas field. *Geophysical Journal International*, 218(3), 1781–1795. https://doi.org/10.1093/gji/ggz237

Cho, I., & Iwata, T.(2019). A Bayesian approach to microtremor array methods for estimating shallow S wave velocity structures: Identifying structuralsingularities. *Journal of Geophysical Research: Solid Earth*, 124, 527–553. https://doi.org/10.1029/2018JB015831

D'Amico, V., Picozzi, M., Baliva, F., & Albarello, D.(2008). Ambient noise measurements for preliminary site-effects characterization in the urban area of Florence, Italy. *Bulletin of the Seismological Society of America*, 98(3): 1373–1388. https://doi.org/10.1785/0120070231

Ekström, G., Abers, G. A., & Webb, S.C.(2009). Determination of surface-wave phase velocities across USArray from noise and Aki's spectral formulation. *Geophysical Research Letters*, 36(18), 5, L18301–9. https://doi.org/10.1029/2009GL039131

Forchap, E.A., & Schmid, G.(1998). Experimental determination of Rayleigh-wave mode velocities using the method of wavenumber analysis. *Soil Dynamics and Earthquake Engineering*, 17: 177–183.

Forbriger, T.(2003a). Inversion of shallow-seismic wavefields: I. Wavefield transformation. *Geophysical Journal International*, 153, 719–734.

Forbriger, T.(2003b). Inversion of shallow-seismic wavefields: II. Inferring subsurface properties from wavefield transforms. *Geophysical Journal International*, 153, 735–752.

Foti, S., Parolai, S., Albarello, D., & Picozzi, M.(2011). Application of surface-wave methods for seismic site characterization. *Surveys in Geophysics*, 32(6), 777–825. https://doi.org/10.1007/s10712-011-9134-2

Gabriels, P., Snieder, R. & Nolet, G.(1987), In situ measurements of shear-wave velocity in sediments with higher-mode Rayleigh waves. *Geophysical Prospecting*, 35 :187-196

Ganji, V., Gucunski, N., & Nazarian, S.(1998). Automated inversionprocedure for spectral analysis of surface waves. *Journal of Geotechnical and Geoenvironmental Engineering, ASCE*, 124(8): 757–770.

Gerstoft, P., & Tanimoto, T.(2007). A year of microseisms in Southern California. *Geophysical Research Letters*, 34, L20304. https://doi.org/10.1029/2007GL031091

Gucunski, N., & Woods, R.D.(1992). Numerical simulation of the SASW test. *Soil Dynamics and Earthquake Engineering*, **11**:213–227.

Gui, B., He, D., Zhang, Y., Sun, Y., Huang, J. & Zhang, W.(2017). Geometry and kinematics of extensional structural wedges. *Tectonophysics*, 699 :199-212, https://doi.org/10.1016/j.tecto.2017.01.013.

Haney, M.M., Mikesell, T.D. & Van Kasper, W.(2012). Extension of the spatial autocorrelation (SPAC) method to mixed-component correlations of surface waves. *Geophysical Journal International*,191:189–206.

Harkrider, D.G.(1964). Surface waves in multilayered elastic media I. Rayleigh and Love waves from buried sources in a multilayered elastic half-space. *Bulletin of the Seismological Society of America*,54 (2): 627–679.

Harmon, N., Gerstoft, P., Rychert, C.A., Abers, G.A., de La Cruz, M.S., & Fischer, K.M.(2008). Phase velocities from seismic noise using beamforming and cross correlation in Costa Rica and Nicaragua. *Geophysical Research Letters*, 35, L19303. https://doi.org/10.1029/2008GL035387

He, F.B., Xu, X.W., He, Z.J., Zhang, X.L., Liu, L.Y., Zhang, W., Wei, B. & Ni, J.B.(2020). Research on Neogene-quaternary stratigraphic structure and shallow tectonic features in the north section of of Daxing fault zone based on shallow seismic reflection profiling. *Seismology and geology*, 42(4): 893-908. http://www.dzdz.ac.cn/CN/10.3969/j.issn.0253-4967.2020.04.008

Hellinger, S.J., Shedlock, K.M., Sclater, J.G., Ye, H.(1985). The Cenozoic evolution of the North China Basin.*Tectonics*,4(4):343-358

Herrmann, R.B.(2013). Computer programs in seismology: An evolving tool for instruction and research. *Seismological Research Letters*, 84, 1081-1088, doi:10.1785/0220110096

Hu, S., Luo, S., & Yao, H.(2020). TheFrequency-Bessel Spectrograms ofmulticomponent cross-correlationfunctions from seismic ambient noise. *Journal of Geophysical Research: SolidEarth*, 125, e2020JB019630. https://doi.org/10.1029/2020JB019630

Huang, X.M., Wang, L.M., Xu, J., Fang, Z.J., Zhang, X.M., Xiang, J.C. & Wang, H.(1991). Characteristics of neotectonics movement in Beijing area. *Seismology and Geology (in Chinese)*, 13(1): 43-51.

Huang, J.L. & Zhao, D.P.(2004). Crustal heterogeneity and seismotectonics of the region around Beijing, China. *Tectonophysics*, 385:159-180

Ibs-von Seht, M., & Wohlenberg, J.(1999). Microtremor measurements used to map thickness of soft sediments. *Bulletin of the Seismological Society of America*, 89(1), 250–259.

Lai, V.H., Graves, R.W., Yu, C., Zhan, Z., & Helmberger, D.V.(2020). Shallow basin structure and attenuation are key to predicting long shaking duration in Los Angeles Basin. *Journal of Geophysical Research: Solid Earth*, 125, e2020JB019663. https://doi.org/10.1029/2020JB019663

Lei, X., Qi, B., Guan, W., Zhao, Y., Du, D., Yan, G.X., Liu, H.W. & You, Z.X.(2021). Research on the faults identification based on gravity anomaly in Beijing plain. *Chinese Journal of Geophysics*(in Chinese),64(4): 1253-1265,doi: 10.6038/cjg2021O0210

Liu, B.J., Hu, P., Meng, Y.Q., Feng, S.Y., Shi, J.H. & Ji,J.F.(2009). Research on fine crustal structure using deep seismic reflection profile in Beijing region.*Chinese Journal Of Geophysics*(in Chinese),52(9): 2264-2272,doi: 10.3969/j.issn.0001-5733.2009.09.010

Liu B.J., Zhang X.K., Chen, Y., Feng, S.Y., Ji, J.F., Yuan, H.K. & Zuo, Y.(2011). Research on crustal structure and active fault in the Sanhe-Pinggu Earthquake (*M*8.0) Zone based on single-fold deep seismic reflection and shallow seismic reflection profiling.*Chinese Journal Of Geophysics*(in Chinese),54(5): 1251-1259,doi: 10.3969/j.issn.0001-5733.2011.05.014

Lobkis, O, and Weaver, R.(2001). On the emergence of the Green's function in the correlations of a diffuse field. *Journal of the Acoustical Society of America*, 110:3011–3017.

Löer, K., Riahi, N. & Saenger, E.H.(2018). Three-component ambient noise beamforming in the Parkfield area. *Geophysical Journal International*, 2018,213:1478-1491

Lu, L. Y.(2021). Revisiting the cross-correlation and SPatialAutoCorrelation (SPAC) of the seismic ambient noise based on the plane wave model. *Reviews of Geophysics and Planetary Physics*, 52(2): 123-163

Lu, L. & Zhang, B.(2004), The analysis of dispersion curves of Rayleigh waves in frequency-wavenumber domain. *Canadian Geotechnical Journal*, 41:583-598.

Lu, L., Wang, K. & Ding, Z.(2018). The effect of uneven noise source and/or station distribution on the estimation of azimuth anisotropy of surface waves. *Earthquake Science*, 31(4):175-186

McMechan, G.A., & Yedlin, M.J.(1981). Analysis of dispersivewaves by wave field transformation. *Geophysics*, 46(6): 869-874.

Nafe, J. E., & Drake,C.L. (1963). Physical properties of marine sediments, in The Sea, vol. 3, edited by M. N. Hill, pp. 794 – 815, Interscience, New York.

Nakamura, Y. (1989). A method for dynamic characteristics estimation of subsurface using microtremor on the ground surface. *Railway Technical Research Institute, Quarterly Reports*, 30(1), Article 1.25-33

Nakamura, Y. (2019). What is the Nakamura method? *Seismological Research Letters*, **90** (4): 1437–1443. https://doi.org/10/ghq6p8

Nimiya, H., Ikeda, T., & Tsuji, T. (2020). Three-dimensional S wave velocity structure of central Japan estimated by surface-wave tomography using ambient noise. *Journal of Geophysical Research: Solid Earth*, 123. https://doi.org/10.1029/2019JB019043

Ohori, M., Nobata, A. & Wakamatsu, K.(2003). A Comparison of ESAC and FK Methods of Estimating Phase Velocity Using Arbitrarily Shaped Microtremor Arrays. *Bulletin of the Seismological Society of America*, 2002;; 92 (6): 2323–2332.
doi: https://doi.org/10.1785/0119980109

Olsen, K.(2000). Site amplification in the Los Angeles basin from three dimensional modeling of ground motion. *Bulletin of the Seismological Society of America*, 90(6B),S77–S94.

Park, C.B., Miller, R.D., & Xia, J. (1999). Multichannel analysis of surface waves. *Geophysics*, 64(3), 800–808.

Peng, F., Wang, W. & Kou, H.(2020). Microtremer H/V spectral ratio investigation in the Sanhe-Pinggu area: site responses, shallow sedimentary structure, and fault activity revealed. *Chinese Journal of Geophysics*(in Chinese), 63(10): 3775-3790,doi: 10.6038/cjg2020O0025

Rost, S.,& Thomas, C.(2002). Array seismology:Methods and applications. *Reviews of Geophysics*, 40(3), 2–1–2-27. https://doi.org/10.1029/2000RG000100

Roux, P., & Ben-Zion, Y.(2017). Rayleigh phase velocities in southern California from beamforming short-duration ambient noise, *Geophysical Journal International*, 211(1):450-454

Ruigrok, E., Gibbons, S., &Wapenaar, K.(2017). Cross-correlation beamforming. *Journal of Seismology*, 21(3), 495–508. https://doi.org/10.1007/s10950-016-9612-6

Salomón, J., Pastén, C., Ruiz, S., Leyton, F., Sáez, M., Rauld, R.(2021). Shear wave velocity model of the Abanico Formation underlying the Santiago City metropolitan area, Chile, using ambient seismic noise tomography. *Geophysical Journal International*, Volume 225, Issue 2, May 2021, Pages 1222–1235, https://doi.org/10.1093/gji/ggaa600

Shah, A.K., & Boyd, O.S.(2018). Depth to basement and thickness of unconsolidated sediments for the western United States—Initial estimates for layers of the U.S. Geological Survey National Crustal Model.*U.S. Geological Survey Open-File Report 2018-1115*, 13pp, https://doi.org/10.3133/ofr20181115.

Tokimatsu, K., Tamura, S., & Kojima, H. (1992). Effects of multiple modes on Rayleigh wave dispersion characteristics. *Journal of Geotechnical Engineering*, 118(10), 1529–1543. https://doi.org/10.1061/(ASCE)0733-9410(1992)118:10(1529)

Tsai, V. C. & Moschetti, M. P.(2010). An explicit relationship between time-domain noise correlation and spatial autocorrelation (SPAC) results. *Geophysical Journal International*, 2010,182(1):454-460.

Wang, K., Lu, L., Maupin, V., Ding, Z., Zheng, C., & Zhong, S.(2020). Surface wave tomography of northeastern tibetan plateau using beamforming of seismic noise at a dense array. *Journal of Geophysical Research: Solid Earth*, 125, e2019JB018416.

Wang, J., Wu, G., & Chen, X.(2019). Frequency-Bessel transform methodfor effective imaging of higher-modeRayleigh dispersion curves fromambient seismic noise data. *Journal of Geophysical Research: Solid Earth*, 124,3708–3723. https://doi.org/10.1029/2018JB016595

Wang, Y., Lin, F.C., Schmandt, B., & Farrell, J (2017). Ambient noise tomography across Mount St. Helens using a dense seismic array. *Journal of Geophysical Research:Solid Earth*, 122, 4492–4508. https://doi.org/10.1002/2016jb013769

Wapenaar, K. (2004). Retrieving the elastodynamic Green's function of an arbitrary inhomogeneous medium by cross correlation. *PhysicalReview Letters*, 93, 254301. https://doi.org/10.1103/PhysRevLett.93.254301

Xia, J.H., Miller, R.D., Park, C.B. & Tian, G.(2003). Inversion of high frequency surface waves with fundamental and higher modes, *Journal of Applied Geophysics*, 52:45-57

Xu, X.W., Han, Z.J., Yang, X.P., Zhou, B.G., Li, F., Ma, B.Q., Chen,G.H. & Ran, K.Y.2016. Seismotectonic map in China and its adjacent regions. Beijing: Seismological Press (in Chinese). doi: 10.12031/activefault.china.250.2016.db.

Yamaya, L., Mochizuki, K., Akuhara, T., & Nishida, K.(2021). Sedimentary structure derived from multi-mode ambient noise tomography with dense OBS network at the Japan Trench. *Journal of Geophysical Research: Solid Earth*, 126, e2021JB021789. https://doi. org/10.1029/2021JB021789

Yao, H., van Der Hilst, R.D., & De Hoop, M.V. (2006). Surface-wave array tomography in SE Tibet from ambient seismic noise andtwo-station analysis—I. Phase velocity maps. *Geophysical Journal International*, 166(2), 732–744.

Ye, H., Shedlock, K. M., Hellinger, S.J. & Sclater, J.G.(1985). The North China Basin: An example of a Cenozoic rifted intraplate basin. *Tectonics*, 4(2):153-169